Minerals Engineering 202 (2023) 108263

Contents lists available at ScienceDirect

Minerals Engineering

journal homepage: www.elsevier.com/locate/mineng

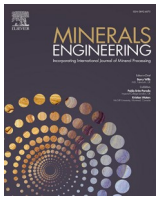

# Isothermal oxidation kinetics of industrial South African chromite concentrates in air

Stefan Swanepoel [a,b], Andrie M. Garbers-Craig [b,*]

[a] Samancor Chrome, Cullinan Place, Morningside, Sandton 2196, South Africa
[b] Centre for Pyrometallurgy, Department of Materials Science and Metallurgical Engineering, University of Pretoria, Pretoria 0002, South Africa

ARTICLE INFO

*Keywords:*
Isothermal oxidation kinetics
Chromite concentrate
Reaction mechanism
Activation energy

ABSTRACT

The oxidation of chromite pellets prior to smelting in a submerged arc furnace is key to ensuring that maximum benefit can be derived in the subsequent smelting step. Oxidized pellet feed material reduces operating costs by increasing energy and reductant efficiency, as well as increasing chrome recoveries.

There is significant compositional variance in chromites used in South African chromite smelting operations due to the different seams from which the materials are mined. The impact of these variances on the extent and rate of oxidation of chromite ores has not been studied before, and it was the impetus for this study.

A detailed kinetic study was carried out on three different types of chromite ores, originating from different commercially mined seams in South Africa, specifically the UG2, LG6 and MG seams. Thermogravimetric analysis was performed on these samples in air at temperatures ranging from 873 to 1473 K, which was used as input to the kinetic analysis. The proposed mechanism of chromite oxidation was found to occur in two stages: initially by random nucleation and growth of a sesquioxide phase, followed by a three-dimensional diffusion-controlled mechanism. The activation energy for oxidation was found to be similar for UG2 and LG6 ore, but higher for MG at all tested temperatures.

The effect of chromite composition, temperature, and time on the extent of oxidation (α) was further quantified and captured in a single regression equation, confirming that time and temperature increase the extent and rate of oxidation. The Ti content was found to be directly correlated with higher values of α for a given time and temperature. The regression equation partially resembles the functional form of the diffusivity equation for cations in chromite found in the literature. It was also found that the distribution between Cr and Al impedes oxidation, with higher Cr content resulting in lower values of α for a given time and temperature.

## 1. Introduction

Stainless steel is used in various applications by many industries (Dishwar et al., 2020) due to its excellent corrosion prevention properties. Chromium is the alloying element responsible for these corrosion properties, and the only commercially recoverable source of chromium is chromite ore (Koleli & Demir, 2016). Chromite belongs to the spinel group of minerals and is a complex solid solution phase with the chemical formula $AB_2O_4$ where A = $Mg^{2+}$, $Fe^{2+}$, etc. and B = $Cr^{3+}$, $Al^{3+}$, $Fe^{3+}$, etc. (Kharbish, 2018). Chromite ore cannot be added to stainless steel directly, therefore the ore is reduced carbothermically to a ferrochrome alloy to concentrate the Cr and remove Mg and Al. Carbothermic reduction is usually achieved in submerged electric arc furnaces (SAF), where specific energy consumption can be as high as 4.8 MWh per ton of ferrochrome (Yu & Paktunc, 2018). Oxidative roasting of chromite, however, can alter the crystal structure of chromite by forming a new sesquioxide phase ($M_2O_3$ with M = $Fe^{3+}$,$Al^{3+}$,$Cr^{3+}$), which can improve the subsequent reduction kinetics (Zhao & Hayes, 2010). Oxidation of $Fe^{2+}$ in chromite to $Fe^{3+}$ prior to smelting has the dual benefit of using CO present in SAF off-gas as reductant, while also allowing iron oxide reduction reactions to start at lower temperatures (Du Preez et al., 2019; Erasmus, 1995). It is, therefore, not surprising that an oxidizing pre-treatment is recommended for South African chromite concentrate (Beukes et al., 2010; Kleynhans et al., 2017).

Many researchers have studied the oxidative pre-treatment of chromite. Tathavakar et al. (2005) found that South African chromite spinel underwent complex phase transformations during oxidation and proposed that the final composition of the spinel depends on the kinetics of

* Corresponding author.
*E-mail addresses:* Stefan.Swanepoel@tuks.co.za (S. Swanepoel), Andrie.Garbers-Craig@up.ac.za (A.M. Garbers-Craig).

https://doi.org/10.1016/j.mineng.2023.108263
Received 23 February 2023; Received in revised form 17 July 2023; Accepted 18 July 2023
Available online 3 August 2023

two reaction steps, both depending on oxygen partial pressure. One reaction involves the redissolution of a Fe-rich maghemite phase that formed during initial oxidation, and the second reaction involves further oxidation of $Fe^{2+}$ into a stable sesquioxide compound.

Borra et al. (2010) investigated the oxidation of chromite ore from the Sukinda region in India between 1073 and 1173 K, confirming the formation of $Fe_2O_3$-rich sesquioxide during oxidation in increasing amounts as temperature and residence times increased. Kapure et al. (2010) found that when ore from the Sukinda region in India was first exposed to two hours of pre-oxidation at 1173 K, the degree of Fe and Cr metallization was subsequently improved when reducing with coal. Biswas et al. (2018) investigated the oxidation kinetics of 4–8 mm pellets produced from Sukinda chromite concentrate between 973 K and 1273 K and found that the phase transformation of chromite spinel to sesquioxide phase was governed by oxidation of $Fe^{2+}$ into $Fe^{3+}$ ions. They found that the best fit for a kinetic model was one of mixed control, both chemical and diffusion control, and the activation energy for the Indian ores were determined to be 65 kJ/mol for the temperature range studied.

Zhu et al. (2016a) studied the oxidation behavior of magnetite from north-eastern China and South African chromite pellets (~10 mm diameter) between 1073 K and 1223 K, determining that the activation for chromite oxidation was almost double that of magnetite oxidation (65.74 kJ/mol vs. 38.74 kJ/mol). They found that the oxidation of high FeO chromite spinel resulted in preferential formation of Fe-rich sesquioxide at low temperatures and thereafter a Cr-rich sesquioxide phase forms on the Fe-rich substrate at higher temperatures.

Studies on 10 mm pellets made from South African chromite from the UG2 seam (Kleynhans et al., 2017; Kleynhans et al., 2016) suggested that oxidative roasting above 1373 K might result in the formation of free $Cr_2O_3$, which would be detrimental to subsequent reduction processing steps. Other studies using South African concentrates in pellets found no evidence of free $Cr_2O_3$ formation, but only detected evidence of oxidation above 1273 K (Ye & Wu, 2018).

A variable that is often understated in literature relating to industrial chromite oxidation is the influence of the seam from where the chromite concentrates were sourced. South African chromite ore, typically from the Lower Group (LG), Middle Group (MG) and Upper Group (UG) seams (Bachmann et al., 2019) influences the elemental and mineralogical composition of the spinel phase as well as the gangue constituents. It is known that the source of magnetite concentrate can affect its oxidation behavior (Cho & Pistorius, 2011), while the elemental distribution in magnetite spinel is also known to influence oxidation behavior (Gillot et al., 1980; Gillot et al., 1976). Previous work by the authors revealed that the oxidation behavior of chromite spinel under industrial conditions is similarly influenced by its crystal composition (Swanepoel et al., 2022). During isochronal heating in air up to 1423 K, it was found that South African chromite concentrates with the lowest Cr:Al ratio experienced the steepest rate of mass change during oxidation while the total fraction of sesquioxide formed was positively correlated to the total Fe content. The kinetics of the reactions were, however, not explicitly studied.

From the reviewed literature, there are different reaction mechanisms occurring over a wide range of temperatures. However, a clear differentiation between South African concentrates originating from different seams is not evident. Furthermore, kinetic investigations for South African concentrates were performed mainly for pellets, as opposed to raw ore particles. Kinetics at pellet scale are influenced by physical properties that may be distinct from the ore source such as pellet porosity, size of particles within the pellet, and gas diffusion through the pellet (Ajersch, 1987; Bonalde et al., 2005). In this study, a series of controlled experiments were performed to study the isothermal kinetics of South African chromite from three of the main mining seams, at the particle scale, over a wide range of temperatures using thermogravimetric analysis (TGA) in air. Classical kinetic models were used to inspect the overriding mechanism of oxidation. The understanding of the oxidation process and the relative mechanism is important for industrial chromite pre-oxidation processes and also for basic research on chromite particle oxidation.

## 2. Brief overview of solid-state oxidation kinetics pertinent to this study

### 2.1. Kinetics in solids

Kinetics in homogeneous phases, such as solutions or gases, is commonly described through the use of the Arrhenius equation, which was empirically developed and later theoretically justified (Logan, 1982; Peleg et al., 2012). Solid-state kinetics evolved from homogenous kinetic principles, although there are factors such as particle size, geometric shape, and interface advance that are unique to heterogenous reactions (Šesták & Berggren, 1971). Although the use of the Arrhenius equation in solid-state kinetics has been criticized (Garn, 1988), its use has also been satisfactorily justified (Galwey & Brown, 2002). For solid state reactions, the concept of concentration of products is not meaningful for describing reaction rates as the heterogeneity implies that reactivity is not the same throughout the sample and expressions of concentration do not relate to reactivity (Brown et al., 1980). Solid-state kinetics where the reaction involves mass loss or gain can be studied using thermal analytical methods, such as thermogravimetry (TGA). The measured change in mass is typically converted to a normalized conversion fraction, α, which ranges from 0 to 1 and is a measure of the progress of the reaction as a function of time or temperature (Brown, 2001). In the case of isothermal thermogravimetric analysis, this conversion fraction at any time is given by the following expression:

$$\alpha = \frac{m_0 - m_t}{m_0 - m_\infty} \tag{1}$$

where $m_0$ is the initial sample mass, $m_t$ is the sample mass at time $t$, and $m_\infty$ is the final sample mass.

The rate of a solid-state reaction can then be defined by the following general equation:

$$\frac{d\alpha}{dt} = A\exp\left(-\frac{E}{RT}\right)f(\alpha) \tag{2}$$

where $f(\alpha)$ is a function describing the reaction model that depends on the reaction mechanism (Gotor et al., 2000), $E$ the activation energy, $A$ the pre-exponential Arrhenius factor, $R$ the universal gas constant and $T$ the temperature. Practically, the reaction model represents the dependence of the reaction on the conversion extent. It is common practice to estimate the reaction model by using a model fitting method (Ghafarinazari et al., 2016). In this method, the experimental data is compared with typical kinetic models and the goodness of fit is evaluated using the coefficient of linear correlation ($r$) (Vyazovkin et al., 2011). Typical reaction types and corresponding forms of $f(\alpha)$ are provided in Table 1.

### 2.2. The Avrami-Erofeev model

The Avrami equation is frequently used to describe the crystallization kinetics for polymers, metals, and glasses (Dimitra & Konstantinos, 2021), and is also typically used to analyze isothermal kinetics (Lv et al., 2017). The model has been named after a number of scientists who independently published and developed the derivation, which is well reviewed by Christian (2002) and Fanfoni and Tomellini (1998). The model is also referred to as the Avrami-Erofeev model (Lv et al., 2017), the JMA model (Sheu et al., 2009), the JMAK model (Fanfoni & Tomellini, 1998), the KEKAM model (Gorbachev, 1981); and the KJMA model (Krüger, 1993) in published works. In this work the model will be referred to as the Avrami-Erofeev model since this is a common convention used for relevant industrial mineral oxidation studies. The model describes the degree of conversion, in this case the extent of oxidation α, as a function of time in the following form:

**Table 1**
Typical values for the Avrami-Erofeev kinetic exponent for various solid state reaction processes under isothermal conditions after Khawam and Flanagan (2005) and Lv et al. (2017).

| Kinetic Model | Symbol | Differential form f(α)= (1/k)(dα/dt) | Integral form g(α) = kt | n |
|---|---|---|---|---|
| *Diffusion Model* | | | | |
| 1D diffusion | $D_1(\alpha)$ | $1/2\ \alpha$ | $\alpha^2$ | 0.62 |
| 2D diffusion, bi-dimensional particle shape | $D_2(\alpha)$ | $(-\ln(1-\alpha))^{-1}$ | $(1-\alpha)\ln(1-\alpha)+\alpha$ | 0.57 |
| 3D diffusion, Jander eqn., tri-dimensional particle shape | $D_3(\alpha)$ | $3(1-\alpha)^{2/3}/2(1-(1-\alpha)^{1/3})$ | $(1-(1-\alpha)^{1/3})^2$ | 0.54 |
| 3D diffusion, Ginstling-Brounshtein | $D_4(\alpha)$ | $(3/2(1-\alpha)^{-1/3}-1)$ | $(1-2/3\alpha)-(1-\alpha)^{2/3}$ | 0.57 |
| *Geometrical contraction models* | | | | |
| Phase-boundary reaction, contracting area | $R_2(\alpha)$ | $2(1-\alpha)^{1/2}$ | $1-(1-\alpha)^{1/2}$ | 1.11 |
| Phase-boundary reaction, contracting volume | $R_3(\alpha)$ | $3(1-\alpha)^{2/3}$ | $1-(1-\alpha)^{1/3}$ | 1.07 |
| *Nucleation model* | | | | |
| Random nucleation and subsequent growth (Avrami) | $A_m$ | $m(1-\alpha)[-\ln(1-\alpha)]^{1-1/m}$ | $(-\ln(1-\alpha))^{1/m}$ | |
| Random nucleation and unidimensional growth | $A_1(\alpha)$ | $1-\alpha$ | $-\ln(1-\alpha)$ | 1.00 |
| Random nucleation and subsequent growth | $A_2(\alpha)$ | $2(1-\alpha)(-\ln(1-\alpha))^{1/2}$ | $(-\ln(1-\alpha))^{1/2}$ | 2.00 |
| Random nucleation and subsequent growth | $A_3(\alpha)$ | $3(1-\alpha)(-\ln(1-\alpha))^{2/3}$ | $(-\ln(1-\alpha))^{1/3}$ | 3.00 |

$$\alpha = 1 - \exp(-kt^n) \tag{3}$$

where $k$ is a rate constant; t is time (min); and n is the Avrami-Erofeev exponent. Here, n corresponds to the model function, with typical values for common kinetic models presented in Table 1. The rate controlling step is generally considered to be nucleation for $n > 1.5$, chemical reaction kinetics when n is close to 1, and diffusion when $n < 1$ (Wolfinger et al., 2022), although it should be noted that the transition points are indicative and are not sharply defined for reactions that occur in parallel.

This model can be used even when the data do not fit any of the common models (Hancock & Sharp, 1972) and can be used to evaluate reactions that occur in parallel or series (Monazam et al., 2014). In order to evaluate experimental data, it is convenient to take the natural logarithm of both sides of Equation (3) as follows:

$$\ln(-\ln(1-\alpha)) = n\ln t + \ln k \tag{4}$$

Using Equation (4), it is observed that a plot of ln(-ln(1-α)) versus lnt allows the determination of n and lnk as the respective slope and intercept of a linear fitting line.

### 2.3. Expected kinetic behavior

The presence of two distinct reaction stages during oxidation is expected and has been observed for the oxidation of other $Fe^{2+}$ containing minerals such as ilmenite (Lv et al., 2017) and magnetite (Colombo et al., 1964; Monazam et al., 2014; Sandeep Kumar et al., 2019). A two stage oxidation mechanism for spinels that contain both $Fe^{2+}$ and $Fe^{3+}$ cations has also been described by Gillot et al. (1986). For a single South African chromite studied, Tathavakar et al. (2005) proposed that the initial oxidation of $Fe^{2+}$ promoted the formation of a maghemite-type defective spinel with the initial oxidation of $Fe^{2+}$ effectively resulting in the formation of a new anion lattice along with cationic vacancies. During this stage, $Fe^{2+}$ cations diffuse outward toward the surface of the grain (the solid–gas interface) and are oxidized to $Fe^{3+}$, while the vacancies generated diffuse inward and promote further cation diffusion. Further oxidation was proposed to require higher temperatures and depended on a two-step process: (1) the Fe-rich maghemite phase redissolves to form a chromite solid solution and (2) further oxidation of $Fe^{2+}$ leads to the exsolution of a Fe-rich sesquioxide phase.

## 3. Materials and methods

### 3.1. Raw materials

The three chromite concentrate samples used were obtained from Samancor Chrome. Two of the concentrates originate from single seam mining operations, namely the LG6 and UG2 seams. The third concentrate was sourced from a mine that concurrently and indiscriminately mines the MG1 and MG2 seams due to their proximity, resulting in the commercial concentrate produced being a blend of these seams. These blends are homogenous in nature and no evidence of variation between the chromite crystals could be discerned during characterization. Prior to oxidation, samples were dried at 378 K for 24 h after which the samples were milled to 90% passing size of 212 μm. The particle size distributions of the milled chromite ore samples were confirmed by laser diffraction particle sizing using a Malvern Mastersizer 2000. A diluted suspension of milled material was treated ultrasonically for 60 s prior to the measurement to disperse individual particles without using a chemical dispersant.

### 3.2. Ore characterization

Chemical characterization of samples was performed with a Spectro Arcos inductively coupled plasma optical emission spectrometer (ICP-OES), calibrated against commercial chromite ore standards. The results, expressed as pure oxides with all Fe as FeO, are shown in Table 2. The $Cr_2O_3$ contents were found to be in accordance with the contents of commercial concentrates (Cramer et al., 2004), with the UG concentrate having the lowest $Cr_2O_3$ content.

X-ray diffraction (XRD) analysis was performed for each sample on a PANalytical X'Pert Pro diffractometer to determine the mineral composition. Samples were prepared according to the standardized PANalytical backloading system, using circular sample holders. The samples were scanned in θ–θ configuration with an X'Celerator detector and variable divergence- and fixed receiving slits. The unit was equipped with Fe-filtered Co-Kα radiation (λ = 1.789 Å). Samples were scanned from 5° to 90°, with a step size of 0.008°. Phase quantification and Rietveld refinement were performed using Profex 4.3.2a (Doebelin & Kleeberg, 2015), $R_{wp}$ values were below 4% which is considered acceptable. The results for the refinement are shown in Table 3, and were in alignment with the ICP-OES results.

Concentrates, prior to milling, were studied on a scanning electron microscope (SEM) coupled with energy-dispersive X-ray spectroscopy (EDS). Samples were cast in resin with the aid of vacuum impregnation, and after polishing were sputter coated with gold for 60 s at 25 mA to achieve a coating of approximately 6 nm. The SEM used was a JEOL IT300 with an iXMAX50 Si-drifted EDS detector. A chemically pure $Fe_2O_3$ sample was used to check the accuracy of EDS results. Spectra were collected with 40 s of live time and 10 scans per phase were performed to allow for average elemental concentrations to be calculated. A working distance of 11 mm and accelerating voltage of 15 kV was used throughout to perform the analysis. In particular, the chromite crystals were analysed in order to calculate the $Fe^{2+}$ and $Fe^{3+}$ concentrations from microprobe analyses using the equation recommended by Droop (1987). In the work by Droop, it was shown that it is possible to calculate

**Table 2**
Results of ICP-OES analysis of ore samples.

| | | ICP-OES Results (Mass %) | | | | | | | | | |
|---|---|---|---|---|---|---|---|---|---|---|---|
| **Label** | **Seam** | **$Al_2O_3$** | **CaO** | **$Cr_2O_3$** | **FeO** | **MgO** | **MnO** | **$SiO_2$** | **$TiO_2$** | **Total** | **mCr:mFe** |
| MG | MG1&2 | 14.87 | 0.15 | 44.07 | 25.92 | 9.35 | 0.22 | 1.70 | 0.73 | 97.03 | 1.50 |
| LG | LG6 | 15.44 | 0.08 | 44.16 | 25.81 | 9.50 | 0.21 | 0.88 | 0.69 | 96.80 | 1.51 |
| UG | UG2 | 15.34 | 0.42 | 39.70 | 26.06 | 10.46 | 0.22 | 4.15 | 0.93 | 97.32 | 1.34 |

**Table 3**
XRD Rietveld refinement results.

| | Refinement Parameters | | Phase Quantities (Mass %) | |
|---|---|---|---|---|
| **Sample** | **Rexp(%)** | **Rwp(%)** | **Chromite** [1] | **Enstatite** [2] |
| MG | 2.27 | 2.83 | 95 | 5 |
| LG | 2.26 | 3.13 | 100 | |
| UG | 2.25 | 3.31 | 90 | 10 |

1 $(Al_{0.001},Fe^{2+}_{0.595},Fe^{3+}_{0.036},Mg_{0.356},Mn_{0.009},Zn_{0.003})[Al_{0.621},Fe^{2+}_{0.038},Fe^{3+}_{0.152},Mg_{0.070},Cr_{1.073},Ni_{0.005},Ti_{0.032},V_{0.010}]O_4$.
2 $(Mg,Fe)SiO_3$.

the number of $Fe^{3+}$ cations per $X$ oxygens in the mineral formula ($F$) as follows:

$$F = 2X\left(1 - \frac{C}{S}\right) \quad (5)$$

where $C$ is the expected (ideal) number of cations per formula unit, and S is the observed total cations per X oxygen atoms calculated from microprobe analysis, when assuming all the iron is $Fe^{2+}$. For chromite spinel, $X = 4$ and $C = 3$, the calculation results are included in the supplementary data file. A computer aided application developed by Ferracutti et al. (2015) was also used to validate the results obtained from using Droop's formula.

Fig. 1 shows typical chromite grains as observed during SEM investigation, confirming chromite as the main phase with the main gangue component being enstatite, as determined by matching SEM-EDS results with the chemical formulas of the phases identified by the XRD analyses.

The average cation concentrations are summarized in Table 4, and the chromite formulas calculated for the MG, LG and UG ores examined are: $(Fe^{2+}_{0.55},Mg_{0.47})(Cr_{0.59},Fe^{3+}_{0.09},Al_{0.31},Ti_{0.01})_2O_4$, $(Fe^{2+}_{0.53},Mg_{0.47})(Cr_{0.60},Fe^{3+}_{0.07},Al_{0.32})_2O_4$, and $(Fe^{2+}_{0.54},Mg_{0.49})(Cr_{0.55},Fe^{3+}_{0.09},Al_{0.33},Ti_{0.01})_2O_4$, respectively.

### 3.3. Oxidation experiments

The experimental apparatus was a calibrated TA SDT Q600 thermogravimetric analyser (TA Instruments). Isothermal oxidation of the chromite particles was performed on a sample with an initial mass of 5 ± 0.2 mg in an open α-alumina crucible. Samples were heated at an isochronal rate of 10 K $min^{-1}$ in a dynamic nitrogen atmosphere, at a flowrate of 50 mL $min^{-1}$, up to the isothermal hold temperature. Once the hold temperature was reached, gas flow was switched over to dynamic dry air flowing at 50 mL $min^{-1}$. Isothermal oxidation was examined from 873 K to 1473 K in steps of 100 K. Based on published experimental conditions used to study the oxidation kinetics of ilmenite particles (Lv et al., 2017), the hold period for runs at temperatures between 873 and 1073 K was 120 min, 60 min for 1173 K, 45 min for 1273 K and 30 min for the 1273 and 1473 K runs. Oxidation was considered complete when the mass gain reached a peak or plateaued. This was found to occur in under 10 min for all the ores and temperature ranges investigated, with chromite particle oxidation conforming more closely to the oxidation times reported for magnetite particles (Sandeep Kumar et al., 2019).

**Table 4**
Molar cation concentrations for raw ore chromite crystals as determined by SEM-EDS, normalized to four oxygen atoms.

| | MG | | LG | | UG | |
|---|---|---|---|---|---|---|
| | **Average** | **SD** | **Average** | **SD** | **Average** | **SD** |
| Cr | 1.18 | 0.03 | 1.21 | 0.05 | 1.11 | 0.03 |
| Σ Fe | 0.73 | 0.03 | 0.67 | 0.06 | 0.72 | 0.01 |
| Al | 0.61 | 0.02 | 0.65 | 0.06 | 0.66 | 0.03 |
| Mg | 0.47 | 0.02 | 0.47 | 0.06 | 0.49 | 0.01 |
| Ti | 0.01 | 0.01 | 0.00 | 0.01 | 0.02 | 0.01 |
| Sum | 3.000 | | 3.001 | | 2.999 | |
| N | 12 | | 10 | | 10 | |
| Cr/(Cr + Al) | 0.66 | | 0.65 | | 0.63 | |
| Mg/(Mg + $Fe^{2+}$) | 0.46 | | 0.47 | | 0.48 | |
| $X_{Fe2+}=n_{Fe2+}/\Sigma n_{Fe}$ | 0.75 | | 0.79 | | 0.74 | |

N = number of EDS analyses performed, SD = standard deviation.

## 4. Results and discussion

### 4.1. Oxidation fraction and oxidation rate

Chromite oxidation is accompanied by stoichiometric mass gain due to the oxidation of $Fe^{2+}$ to $Fe^{3+}$, in terms of oxidation this is typically

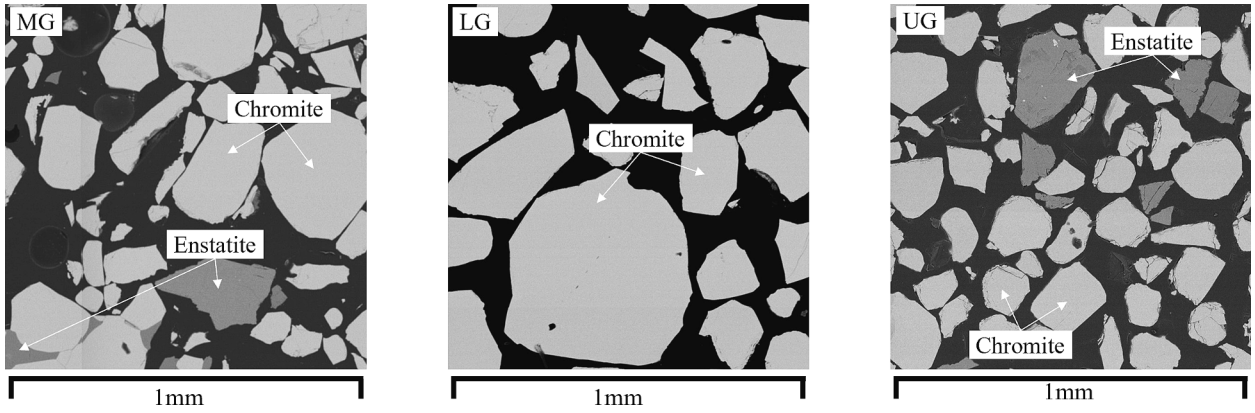


**Fig. 1.** Backscatter electron images of polished chromite ore concentrate samples prior to milling.

approximated as FeO oxidizing to $Fe_2O_3$. The maximum mass gain that chromite particles can achieve is therefore dependent on the initial $Fe^{2+}$ (expressed as FeO) content. For this study, the mass gain measured was normalized with respect to the maximum mass gain captured by TGA during oxidation for each ore type individually, and not the maximum theoretical mass gain, to allow for comparison despite the variation in $Fe^{2+}/Fe^{3+}$ content of the raw ores. The maximum mass gain recorded across all the temperature ranges was therefore assumed to represent full oxidation achievable).

The extent of oxidation (i.e. degree of conversion), or oxidation fraction (α), is defined by:

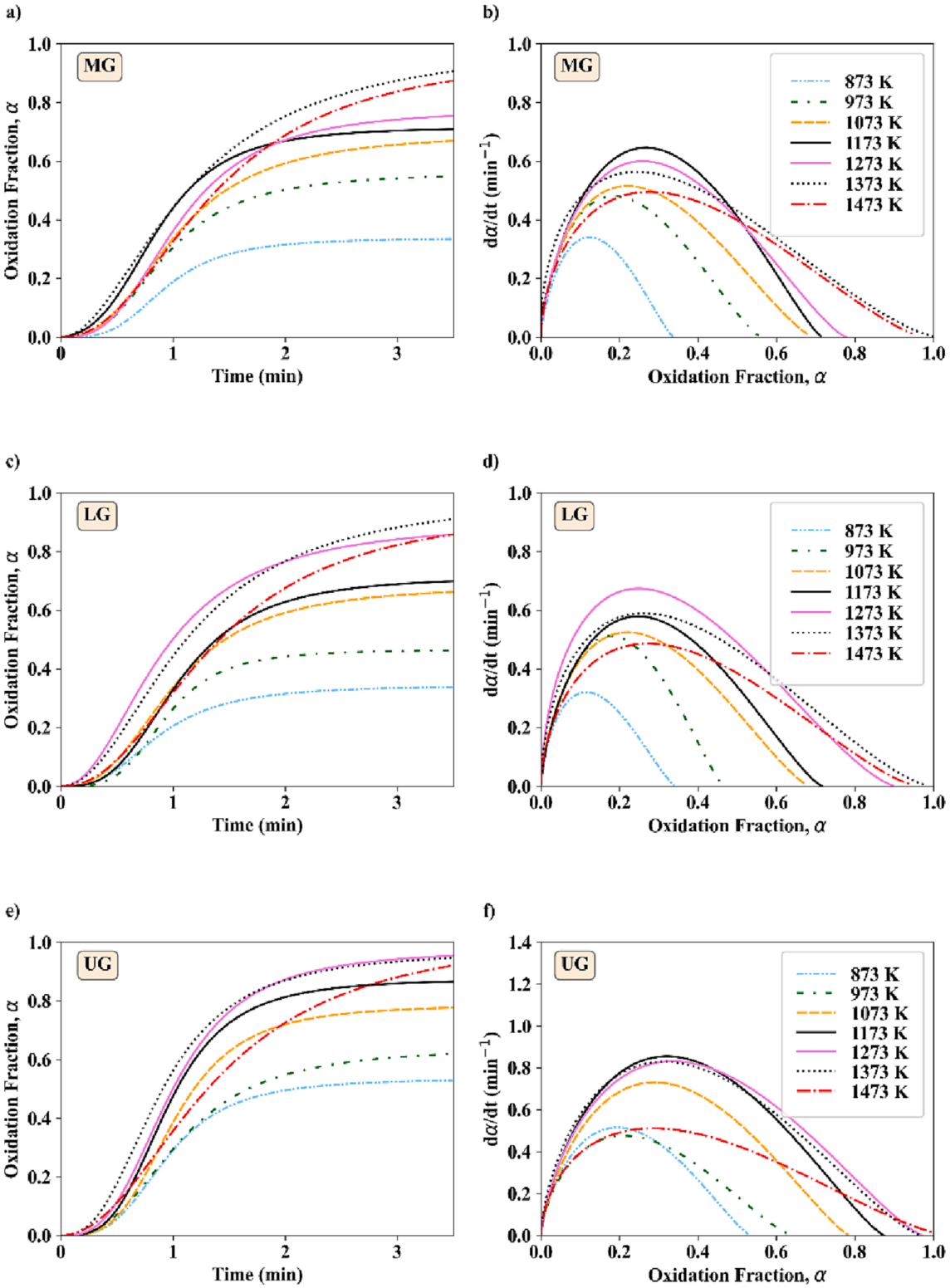


**Fig. 2.** Oxidation fraction (α) with respect to time (a = MG ore, c = LG ore, e = UG ore), and first derivatives of the oxidation fraction with respect to time (dα/dt) versus the corresponding oxidation fraction (b = MG ore, d = LG ore, f = UG ore).

$$\alpha = \frac{\Delta m}{\Sigma m} \quad (6)$$

where $\Delta m$ is the mass increase of the sample, and $\Sigma m$ is the maximum mass increase captured using TGA across the range of temperatures. Each ore type therefore had a unique $\Sigma m$ value. The relationship between oxidation fraction and time with increase in temperature, revealing distinctive sigmoidal curves (Khawam and Flanagan, 2006b) for all ores across the examined temperature range, is shown in Fig. 2 (the time scale has been truncated to focus on the time period during which most oxidation occurred, while extended plots are included in the supplementary materials). It is important to note that the rate of oxidation, reflected by the slope of the oxidation fraction curves in Fig. 2 (a, c and e), changes throughout the reaction process. This behavior is echoed in the calculated first derivatives of the oxidation fraction versus time curves, (Fig. 2 b, d and f), which show that oxidation rates increase up to a maximum value, followed by a continued decrease in reaction rate.

For MG and LG ores, the ultimate oxidation fraction achieved (indicated by the terminal points in Fig. 2b and Fig. 2d) increases with temperature up to 1373 K, at which temperature the maximum oxidation fraction is also observed. When the temperature increases further to 1473 K, the rate of oxidation ($d\alpha/dt$) decreases and the terminal oxidation fraction is lower than what was achieved at 1373 K for the LG and MG ores. For UG ore, the oxidation fraction also increases with temperature, however, the increase between 1273 K and 1373 K is minimal. Therefore, there is little benefit in increasing the oxidation temperature beyond 1273 K for UG ore (Fig. 2e). When the oxidation temperature is increased to 1473 K for UG ore, a significantly lower rate of oxidation is observed compared to the results at 1273 K and 1373 K, while the terminal oxidation fraction is marginally increased (Fig. 2f). The diminished extent and rate of oxidation at elevated temperatures can be attributed to the high-temperature decomposition of the $Fe_2O_3$ product, which is expected to occur above 1473 K (Qu et al., 2014), according to the following chemical reaction:

$$6Fe_2O_3 \rightarrow 4Fe_3O_4 + O_2 \quad (7)$$

Similar high temperature decompositions through the loss of excess oxygen in non-reducing atmospheres has been reported for manganese containing spinels (Gillot et al., 1989), lithium-manganese containing spinels (Thackeray et al., 1996), hematite (Xing et al., 2020) and synthetic chromite (Lughi et al., 2020). In the oxidative roasting of magnetite pellets, high temperatures (>1623 K) are avoided to limit this decomposition reaction, as it is known to result in a loss of pellet quality (Jiang et al., 2008). The target temperatures in the sinter belt during pre-oxidation of chromite are given to be between 1673 and 1773 K (Basson & Daavittila, 2013). At these temperatures, deoxidation is thermodynamically possible, and deoxidation may indeed offer an explanation for the low levels of oxidation reported by Zhao and Hayes (2010) for the examined industrial chromite pellets. As the oxidation reaction has been reported to contribute less to the strengthening of chromite pellets compared to the strength of magnetite pellets (Zhu et al., 2016a), it is not apparent, however, that deoxidation will have the same impact on the quality of chromite pellets.

The oxidation fractions (α) at maximum oxidation rates (d α /dt) are consistently higher for UG ore than for LG and MG ores throughout the examined temperature range (Fig. 3a). This indicates that the oxidation reaction for UG ore progresses further before the reaction starts to slow down. The oxidation fraction at maximum oxidation rate for the UG ore, takes on an approximate parabolic shape between 1073 K and 1473 K, with the peak value at 1273 K. The oxidation rate of the UG2 ore however, increases up to a maximum rate at 1173 K, whereafter a further increase in temperature does not increase its oxidation rate (Fig. 3b). From 1173 K up to 1373 K the oxidation rate remains essentially constant, and then significant decreases when the temperature further increases to 1473 K.

For both LG and MG ores, the oxidation fractions at the maximum oxidation rates increase as the temperature increases to 1073 K, plateau between 1173 K and 1373 K, and then peak at 1473 K (Fig. 3a). In other words, between 1173 K and 1373 K, the rate of reaction peaks at similar oxidation fractions, while at 1473 K the oxidation fraction increases again for the LG and MG ores, although the oxidation rate has slowed down.

The highest oxidation rates for the UG and MG ore were recorded at 1173 K (Fig. 3b), while the highest oxidation rate for the LG ore was recorded at 1273 K. While the maximum oxidation rates for LG and MG ore decrease linearly as the temperature increases further, the oxidation rates for UG ore at 1273 K and 1373 K are only slightly lower than the maximum rate at 1173 K. At 1473 K the maximum oxidation rates were significantly reduced for all three ore samples, reaching rates similar to those observed for UG at 873 K, and for LG and MG at 973 K.

It is significant to note that the maximum oxidation rates of the three ores, as well as their oxidation fractions at maximum oxidation rates, are nearly identical at 1473 K. This demonstrates that the oxidation fractions and oxidation kinetics are not necessarily optimized simply by increasing the temperature, and highlights that the behavior of the UG ore is markedly different from that of the LG and MG ores. An industrial

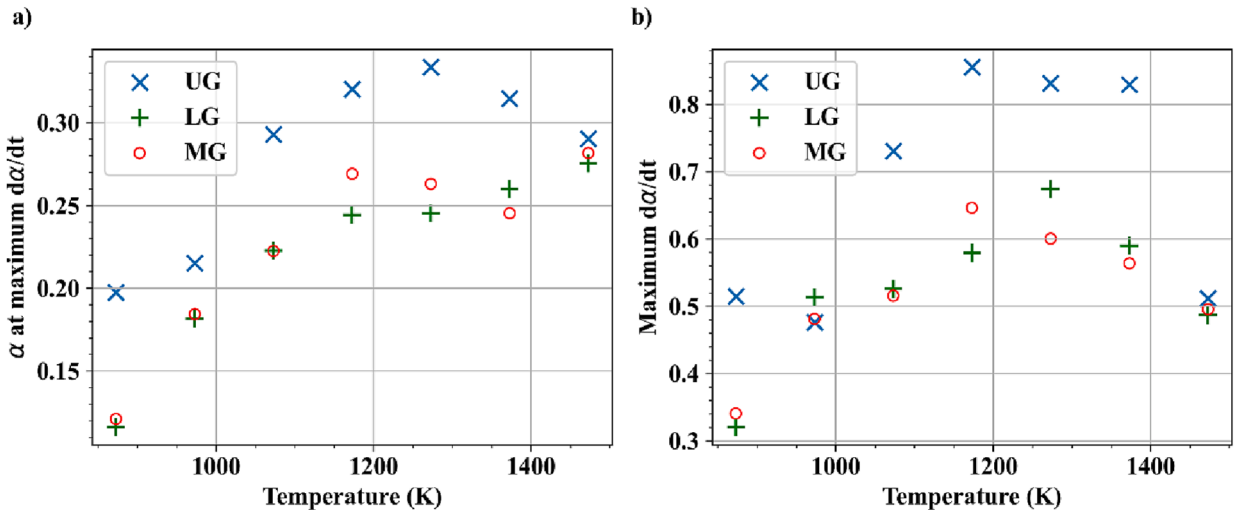


**Fig. 3.** Scatter plots indicating (a) the oxidation fraction (α) at maximum oxidation rate (dα/dt), as a function of temperature; and (b) the corresponding maximum oxidation rates, also as functions of temperature.

temperature profile that is optimized for one ore type will, therefore, not necessarily achieve the same results for a different ore type. Although the behavior observed for the LG and MG ores is similar at 1474 K, there are differences in the temperature range from 1173 K to 1373 K. These differences would make it challenging to design a non-isothermal roasting temperature profile that optimizes oxidation for all ores simultaneously.

The results shown in Fig. 3 also indicate that oxidation can be divided into two stages, namely the initial stage where oxidation rate increases and a second stage where oxidation rate decreases. The relationship between the contribution of these two stages to the ultimate extent of oxidation, as a function of temperature, is shown in Fig. 4. Most of the oxidation occurs during the second stage, where a decreasing rate of oxidation is observed, at all temperatures examined.

To evaluate the reaction kinetics, the individual α versus t plots shown in Fig. 2 (a, c and e) were mathematically transformed into ln(-ln (1-α)) versus lnt plots (equation (4). A selection of these new plots, showing experimental data and linear regression fitting curves for 873 K and 1473 K, is shown in Fig. 5. The lowest and highest temperatures examined are shown to demonstrate that the general form of the Avrami-Erofeev curves did not alter across the temperature range studied. The complete set of fitting parameters are listed in Table 5 (the complete set of Avrami-Erofeev curves is included in the supplementary data). None of the reactions conformed to a single Avrami-Erofeev equation throughout the oxidation reaction at any of the investigated temperatures. Instead, two distinct reaction linear stages were observed, with the transition between the stages and the individual slopes varying with temperature.

Fig. 6 shows a plot of the Avrami-Erofeev exponents for the two linear sections as a function of temperature. Compared to the typical values in Table 1, the plot indicates that the kinetic exponents of the first stage reasonably conform to random nucleation and subsequent growth mechanisms ($n > 1.5$) over the explored temperature range. The exponents of the second stage conform closest to a three-dimensional diffusion model ($n < 0.6$) between 873 K and 1273 K. At 1373 K the exponents for the MG and LG are observed to increase toward a value of approximately 1. At 1473 K the exponent for the UG ore also increases. This indicates that at elevated temperatures there is likely to be a change in the mechanisms and kinetic barriers involved. Although the exponents remain low enough ($n < 1.5$) to rule out random nucleation and subsequent growth models, the range of observed values does not consistently align with any of the values expected in Table 1.Therefore, relying on the broad reaction classification scheme is not sufficient, and another approach is needed to interpret these values. The fluctuation in exponents also suggests that parallel reaction processes are involved during the oxidation of chromite and that the reactions do not occur in series.

Christian (2002) reported typical values for the kinetic exponent that could be obtained under various experimental conditions for diffusion-controlled growth. These values are better suited to interpreting the change in kinetic exponent observed at elevated temperatures during the second stage of oxidation. The abovementioned classification scheme shows that a value of 0.5 may be indicative the thickening of very large plates after complete edge impingement. When the exponent is equal to 1, it is considered typical for the growth of needles and plates with finite long dimensions or the thickening of long needles after complete impingement. When the exponent is between 1 and 1.5, it likely corresponds to the growth of particles that already have appreciable initial volume. The backscatter electron images shown in Fig. 7 confirm the prolific growth of sesquioxide needles in a typical Widmanstätten pattern (Tathavakar et al., 2005; Treffner, 1961) at 1373 K. This aligns with the diffusion-controlled growth mechanism classification proposed by Christian (2002) for the range of Avrami-Erofeev exponents observed during the second stage.

XRD patterns for the raw and oxidised chromite concentrates are shown in Fig. 8, confirming the transformation from chromite to sesquioxide while no evidence of the metastable maghemite phase was detected after the isothermal runs. The closest reference pattern match for the sesquioxide phase was found to be eskolaite ($Cr_2O_3$), however, the phase is a solid solution between $Cr_2O_3$-$Al_2O_3$-$Fe_2O_3$ (Biswas et al., 2018; Zhao & Hayes, 2010) and was confirmed by SEM analysis to not be pure $Cr_2O_3$. These solid solutions are known to have significant overlap in crystal lattice dimensions over the composition range and can therefore not be accurately distinguished using XRD techniques only (Amores et al., 1999).

In summary, the results are in agreement with the expected behavior for the solid-state oxidation of $Fe^{2+}$ in a spinel structured crystal, and suggest that two distinct mechanisms dominate during the oxidation process.

Although it is not possible to fully resolve the nuanced mechanisms of the two stages using only TGA techniques (Zhou et al., 2003), confirming a multi-stage reaction is of interest, as it may be possible to enhance oxidation by altering the process parameters either at low temperatures (Tang et al., 2014) or at high temperatures (Haas et al., 1993).

### 4.2. Evaluation of apparent reaction activation energy using the model-free method

The dynamic reaction rate for isothermal gas–solid reactions is obtained from the first derivative of the conversion fraction (in this case oxidation) with respect to time, as follows:

$$\frac{d\alpha}{dt} = k(T)f(\alpha) \tag{8}$$

where $d\alpha/dt$ is the reaction rate, $k(T)$ is the temperature dependent reaction rate constant, and $f(\alpha)$ is the mathematical description of the

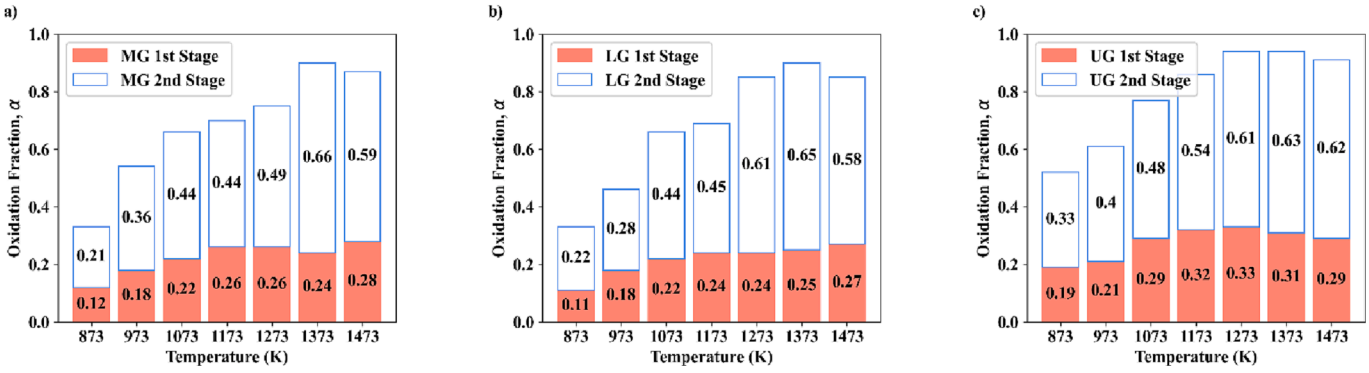


**Fig. 4.** Bar plot of the oxidation fraction during increasing oxidation rate (1st stage) and decreasing oxidation rate (2nd stage) as a function of temperature for (a) MG, (b) LG and, (c) UG ore.

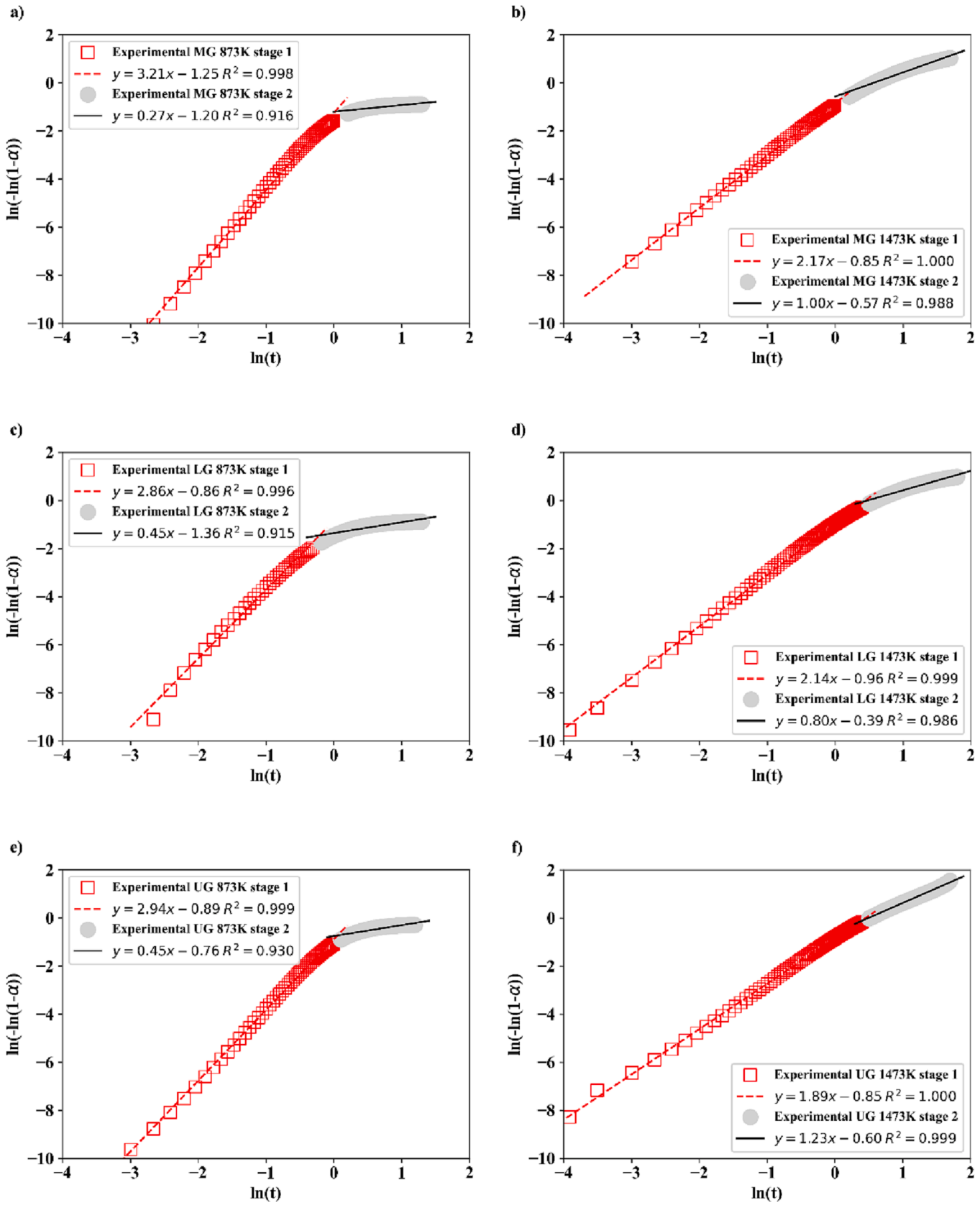


**Fig. 5.** Selected Avrami-Erofeev plots of ln(-ln(1-α)) versus lnt at different temperatures for the ores examined.

**Table 5**
Regression fitting parameters determined by ln-ln analysis at different temperatures.

| Ore | Stage | Parameter * | 873 K | 973 K | 1073 K | 1173 K | 1273 K | 1373 K | 1473 K |
|---|---|---|---|---|---|---|---|---|---|
| UG | First Stage | Slope | 3.215 | 2.696 | 2.460 | 1.895 | 2.620 | 1.845 | 2.173 |
| | | Intercept | −1.25 | −0.69 | −0.74 | −0.57 | −0.78 | −0.44 | −0.85 |
| | | $R^2$ | 0.998 | 0.999 | 0.999 | 0.998 | 0.998 | 0.998 | 1.000 |
| | Second Stage | Slope | 0.273 | 0.496 | 0.469 | 0.322 | 0.278 | 0.913 | 1.001 |
| | | Intercept | −1.20 | −0.77 | −0.47 | −0.16 | −0.06 | −0.31 | −0.57 |
| | | $R^2$ | 0.916 | 0.938 | 0.961 | 0.942 | 0.907 | 0.997 | 0.988 |
| MG | First Stage | Slope | 2.861 | 3.730 | 2.593 | 2.898 | 1.945 | 1.901 | 2.136 |
| | | Intercept | −0.86 | −0.73 | −0.62 | −0.81 | −0.31 | −0.53 | −0.96 |
| | | $R^2$ | 0.996 | 1.000 | 0.999 | 0.999 | 0.997 | 0.998 | 0.999 |
| | Second Stage | Slope | 0.452 | 0.385 | 0.589 | 0.335 | 0.423 | 0.790 | 0.805 |
| | | Intercept | −1.36 | −0.88 | −0.61 | −0.27 | 0.10 | −0.14 | −0.39 |
| | | $R^2$ | 0.915 | 0.880 | 0.945 | 0.908 | 0.967 | 0.994 | 0.986 |
| LG | First Stage | Slope | 2.943 | 2.405 | 3.047 | 2.994 | 2.622 | 2.213 | 1.886 |
| | | Intercept | −0.89 | −1.02 | −0.69 | −0.40 | −0.37 | −0.23 | −0.85 |
| | | $R^2$ | 0.999 | 0.999 | 0.999 | 0.999 | 0.999 | 0.998 | 1.000 |
| | Second Stage | Slope | 0.454 | 0.433 | 0.374 | 0.320 | 0.500 | 0.474 | 1.232 |
| | | Intercept | −0.76 | −0.58 | −0.07 | 0.26 | 0.42 | 0.43 | −0.60 |
| | | $R^2$ | 0.930 | 0.941 | 0.913 | 0.892 | 0.943 | 0.966 | 0.999 |

* Slope = n, Intercept = lnk.

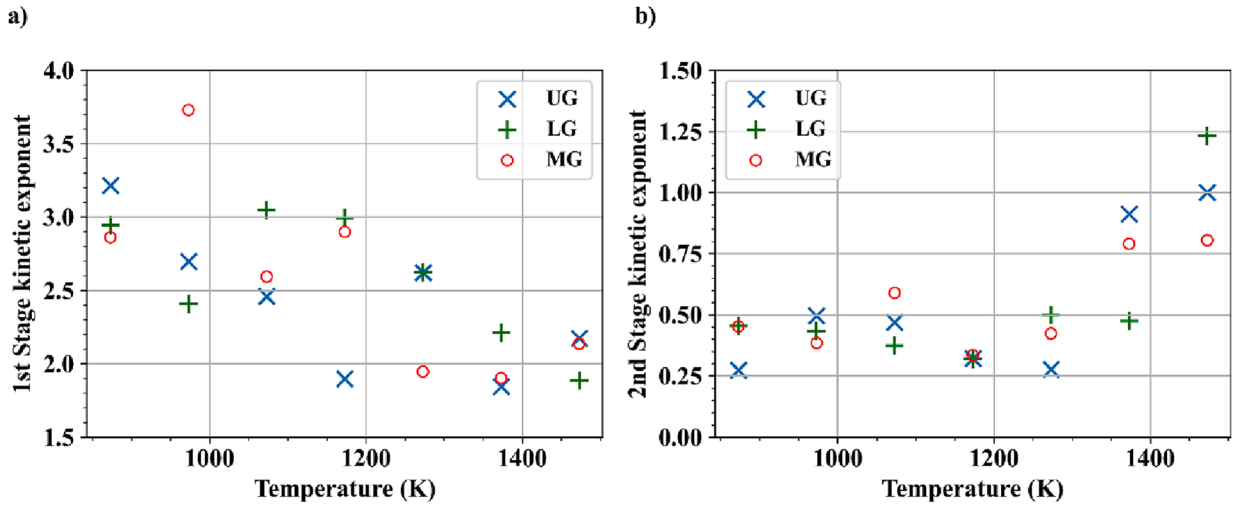


**Fig. 6.** Avrami-Erofeev exponents (n) for (a) the first reaction stage and (b) the second stage as a function of temperature.

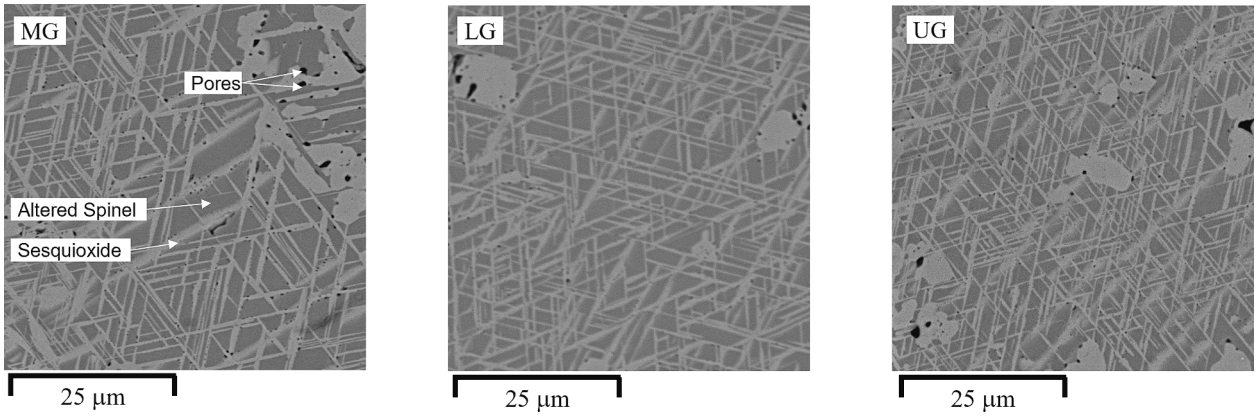


**Fig. 7.** Backscatter electron images of the three ores after isothermal runs at 1373 K, indicating the exsolution of a sesquioxide phase (light grey) in preferential orientation within a spinel matrix (dark grey). Pores (black) are also present in areas where the sesquioxide phase has grown wider than the average Widmanstätten lamellae observed.

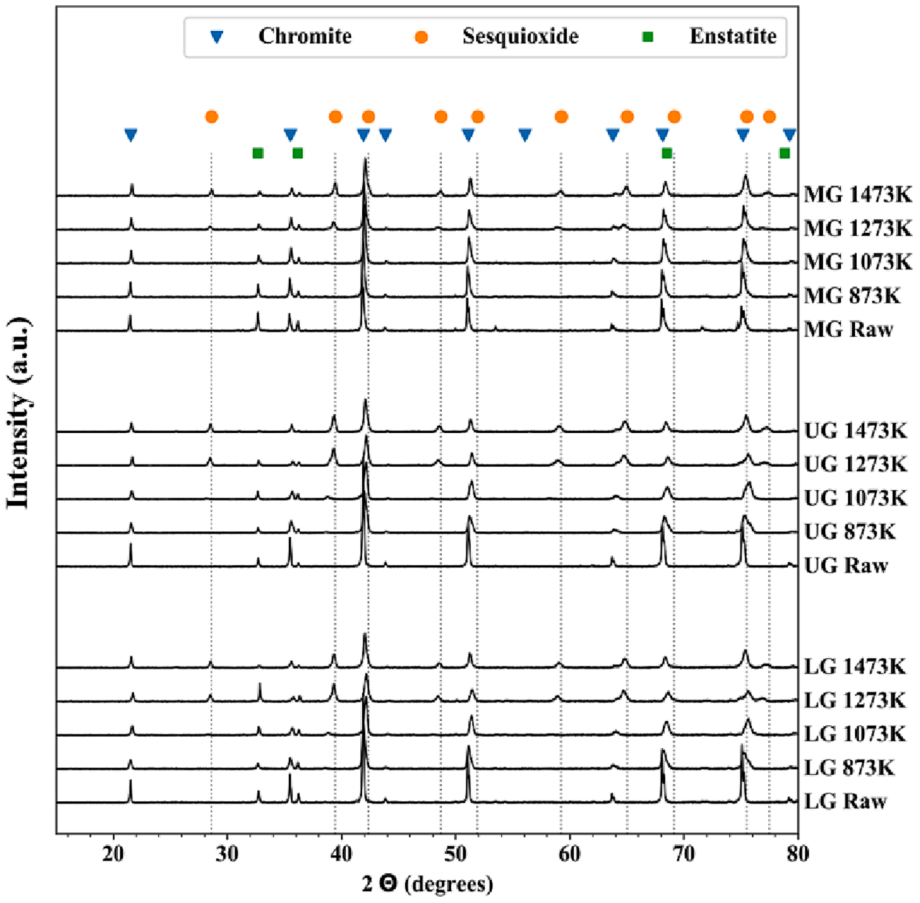


**Fig. 8.** XRD patterns of chromite ores after isothermal runs at different temperatures.

reaction mechanism function. Among the variables, the temperature dependence of *k(T)* satisfies the Arrhenius equation:

$$k(T) = Aexp\left(\frac{-E_\alpha}{RT}\right) \tag{9}$$

where $E_\alpha$ is the apparent activation energy (J $mol^{-1}$), $A$ is the pre-exponential frequency factor ($min^{-1}$), $R$ is the universal gas constant (8.314JK$^{-1}$ $mol^{-1}$), *k(T)* is the overall rate constant ($min^{-1}$), and $T$ is the reaction temperature (K). The combination of Eqs.(8) and (9) leads to Eq.(10) and its logarithmic form in Eq.(11):

$$\frac{d\alpha}{dt} = Aexp\left(\frac{-E_\alpha}{RT}\right)f(\alpha) \tag{10}$$

$$\ln\left(\frac{d\alpha}{dt}\right) = ln(A) - \frac{E_\alpha}{RT} + ln(f(\alpha)) \tag{11}$$

When considering fixed values of α at various isothermal temperatures and setting the reaction model *f(α)* to 1, a model-free *iso*-conversional evaluation can be performed, which assumes that the reaction

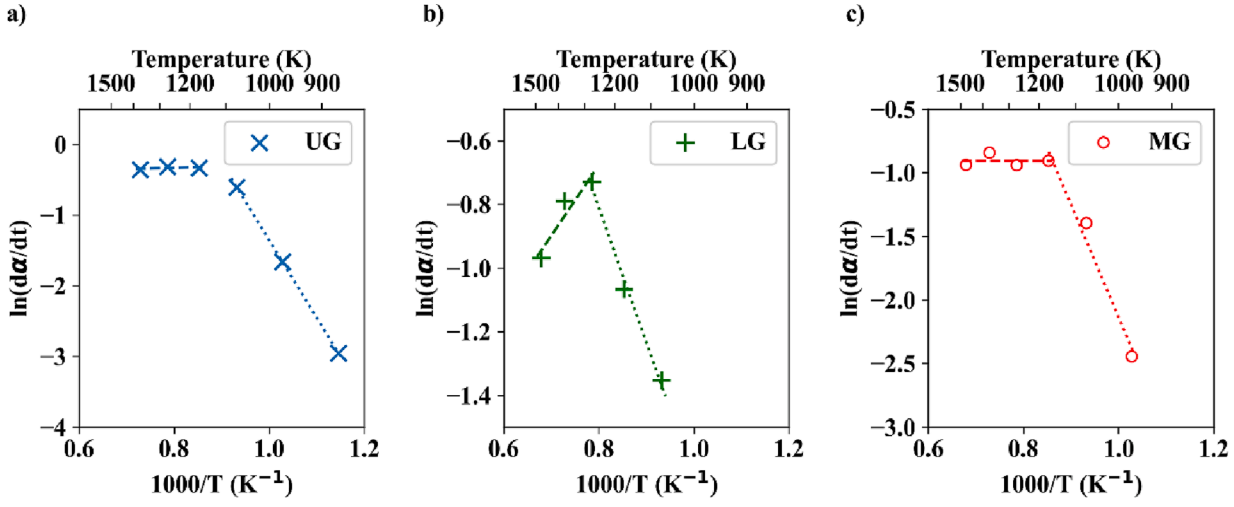


**Fig. 9.** Arrhenius plot for 50% oxidation rate (α = 0.5) of the experimental results for (a) UG ore, (b) LG ore and (c) MG ore.

rate at constant extent of conversion is solely a function of temperature (Vyazovkin et al., 2011). Eq.(11) accordingly indicates that a plot of ln $(d\alpha/dt)$ against $1/T$ will result in the slope being equal to - $E_\alpha$/R enabling the evaluation of $E_\alpha$ for progressive degrees of conversion without any assumptions regarding the form of the underlying model (Friedman, 1964). All *iso*-conversional methods, however, fundamentally assume that the reaction model at a given degree of conversion is not dependent on heating rate or temperature (Vyazovkin & Wight, 1999). To illustrate the methodology used, the Arrhenius plot for 50% oxidation rate is presented in Fig. 9, where $f(\alpha)$ was set to 1, resulting in the model-free fitting method. In accordance with the results of the Avrami-Erofeev plots, two distinct linear regions were observed in the Arrhenius plots.

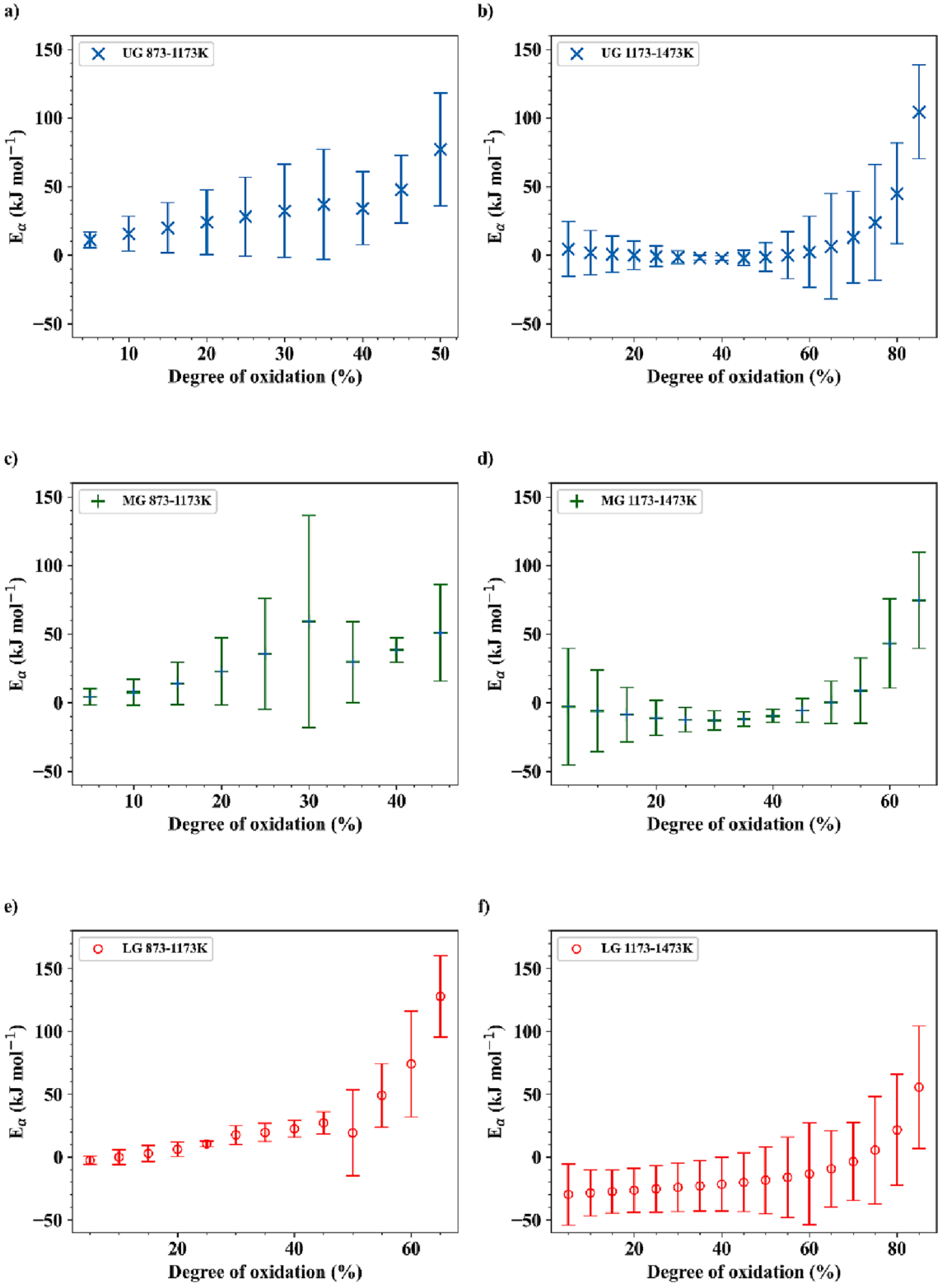


**Fig. 10.** $E_\alpha$ vs α plots for isothermal oxidation runs evaluated by the Friedman *iso*-conversional method, error bars indicate the 95% confidence interval determined for the slopes from the linear regression analyses performed to determine $E_\alpha$.

The first linear region is prevalent from 873 K to 1173 K, while the second linear region was predominant between 1173 K and 1473 K. These regions were taken to be representative of the apparent activation energies for the random nucleation and diffusion mechanisms, respectively.

As demonstrated for $\alpha = 0.5$, linear regression was performed for the entire oxidation range in 5% increments (i.e. $\alpha$ was varied from 0.05 to 1 in steps of 0.05), to determine the range of $E_\alpha$ using the Freidman isochronal method (Fig. 10). For the temperature range between 873 K and 1173 K, the apparent activation energy gradually increases as the extent of oxidation increases. For the UG and LG ores, the apparent activation energy increases at a greater rate once 40% oxidation is exceeded. For the MG ore, extents of oxidation reached at this temperature were not sufficient for activation energies to be evaluated beyond 45% oxidation at the low temperature range. The high variation in activation energy observed for the MG ore at 30% oxidation may be due to an increase in the heterogenous nature of the crystal (Khawam and Flanagan, 2006a) or may indicate a change in reactivity due to intra-crystalline strain, crystal defect formation, or product formation (Galwey, 2003).

In the temperature range between 1173 K and 1473 K, the activation energies are stable up to 45% oxidation, while the activation energies are quite low and even negative. The activation energies, however, start increasing sharply as the extent of oxidation increases beyond the range of 40% to 50%. Due to the variation in $E$ αas the extent of oxidation increases, as well as the range of the 95% confidence intervals, it is not prudent to attempt to report a singular value for activation energy. The values observed, however, are generally lower than the ~ 65 kJ/mol activation energy determined for the oxidation of chromite pellets (Biswas et al., 2018; Zhu et al., 2016a) but exceeded this value once higher extents of oxidation were achieved. The variation in effective activation energy as the extent of conversion increases for a multi-step process is not uncommon, and has been well documented (Dowdy, 1987a, 1987b; Elder, 1984, 1990; Flynn & Wall, 1966). Although negative activation energies are not possible for elementary reactions, in complex reactions studied during solid state kinetics these merely indicate that the reaction rate increases as temperature decreases (Vyazovkin, 2016). This can occur when a kinetic limitation appears at a higher temperature as observed during the oxidation of magnetite (Wolfinger et al., 2022). Such limitations could be as a result of the sintering or agglomeration of solid particles blocking the active sites for a gaseous reactant or the deactivation (blockage) of low resistance diffusion paths due to the formation of oxide (Muraleedharan Nair & Abanades, 2021; Patnaik & Goldfarb, 2016).

As cautioned by Vyazovkin and Wight (1997), care should be taken to interpret Arrhenius parameters for solid state reactions when there are multiple elementary reactions overlapping as there may be interaction due to diffusion, adsorption, desorption and other physical processes. Rather, the Arrhenius parameters are reflective of the effective constants for the overall rate of the oxidation process. The increase in effective activation energy has been observed as oxidation extent increases for competing reactions (Vyazovkin & Lesnikovich, 1990). This phenomenon has been particularly noted in oxygen where competing pyrolysis and oxidation reactions occur (Vyazovkin et al., 1991). Similar observations have been made for the oxidation of hematite (Salmani et al., 2017) and magnetite (Sardari et al., 2017).

In general, one may consider the activation energy to be the threshold (or energy barrier) that needs to be overcome to permit the bond redistribution steps that are required for the transformation of reactants into products. The low initial activation energies during both temperature ranges are congruent with how readily $Fe^{2+}$ is oxidized in air. For the low temperature stage, the curves correspond to an increasing resistance to the reaction as the product layer thickness increases. For the second stage the increase in activation energy during the final stages of oxidation points to an increased energy barrier due to a decrease in the availability of reactants.

Although a single mechanism is difficult to isolate, it is possible to gain some insight into potential mechanisms by considering the range of activation energies identified in previous studies. Relevant to the oxidation of Brazilian chromite, Da Silva et al. (1976) determined that the activation energy for $Fe^{2+}$ oxidation in a tetrahedral site is around 16.7 kJ/mol (between 673 K and 973 K), the activation energy for the diffusion of $Fe^{3+}$ from octahedral to tetrahedral sites is around 71.1 kJ/mol (between 973 K and 1173 K), and the activation energy for the diffusion of $Fe^{3+}$ from tetrahedral to octahedral sites is 196.6 kJ/mol (between 1173 K and 1273 K). The range of activation energies determined in this study largely fall within this range. Comparative activation energies for the diffusion of other cations in spinels and sesquioxides are

**Table 6**
Comparative results for activation energies in spinels and sesquioxides.

| Substrate | Diffusing element / Reaction | Activation Energy (kJ/mol) | Temperature Range | Reference |
|---|---|---|---|---|
| Chromite (Brazil) | Oxidation of tetrahedral $Fe^{2+}$ | 16.7 | 673 – 973 K | (Da Silva et al., 1976) |
| | Diffusion of $Fe^{3+}$ from octahedral to tetrahedral site | 71.1 | 973 – 1173 K | (Da Silva et al., 1976) |
| | Diffusion of $Fe^{3+}$ back to octahedral site | 196.6 | 1173 – 1273 K | (Da Silva et al., 1976) |
| $FeCr_2O_4$ | Cr (Volume Diffusion) | 119.3 ± 29 | 1073 – 1173 K | (Gilewicz-Wolter et al., 2006) |
| | Cr (Grain-Boundary) | 150.8 ± 13 | 1073 – 1173 K | (Gilewicz-Wolter et al., 2006) |
| | Fe (Volume Diffusion) | 225.5 ± 31 | 1073 – 1173 K | (Gilewicz-Wolter et al., 2006) |
| | Fe (Grain-Boundary) | 164.1 ± 12 | 1073 – 1173 K | (Gilewicz-Wolter et al., 2006) |
| $MgAl_2O_4$ | Cr | 306 ± 58 | 1673 – 1923 K | (Stubican & Osenbach, 1984) |
| | Cr | 516 ± 80 | 1673 – 1973 K | (Suzuki et al., 2008) |
| | Cr | 277 ± 37 | 975 – 1150 K | (Posner et al., 2016) |
| | Cr | 219 ± 35 | 950 – 1200 K | (Posner et al., 2016) |
| $CoCr_2O_4$ | Cr | 292 ± 36 | 1673 – 1873 K | (Sun, 1958) |
| $Al_2O_3$ | Al | 477 ± 36 | 1943 – 2178 K | (Paladino & Kingery, 1962) |
| | Al | 510 | 1473 – 1973 K | (Gall et al., 1994) |
| | Cr | 265 | 1473 – 1973 K | (Lesage et al., 1983) |
| | Cr | 290 ± 36 | 1279 – 1773 K | (Moya et al., 1995) |
| | Fe | 300 | 1473 – 1973 K | (Lesage et al., 1983) |
| | $O^{2-}$ | 636 ± 20 | 1773 – 1993 K | (Prot & Monty, 1996) |
| $Fe_2O_3$ | $O^{2-}$ | 405 ± 25 | 1125 – 1350 K | (Reddy & Cooper, 1983) |
| | Fe | 174 | 981 – 1173 K | (Atkinson & Taylor, 1985) |
| | Fe | 579 | 1173 – 1576 K | (Atkinson & Taylor, 1985) |
| $Cr_2O_3$ | $O^{2-}$ | 230 | 1373 K | (Sabioni et al., 1992a) |
| | Cr | 280 | 1473 – 1723 K | (Sabioni et al., 1992b) |
| | Al | 451 | 1373 – 1523 K | (Rothhaar & Oechsner, 1998) |

summarized in Table 6, with the activation energies for $Cr^{3+}$, $Al^{3+}$ and $O^{2-}$ being substantially larger than observed in this study, indicating that diffusion of these species are not rate limiting during oxidation of the chromites studied. Rather, $Mg^{2+}$ and $Fe^{2+}$ diffusion mechanisms are likely to be dominant, which is supported by studies that found that during chromite oxidation the sesquioxide phase formed is enriched in iron but essentially depleted of $Mg^{2+}$ (Kapure et al., 2010; Zhu et al., 2016b).

### 4.3. Impact of spinel composition on oxidation rate

To test the idea that the cation composition has a statistically significant impact on the oxidation behavior of the individual spinels, a multiple linear regression (MLR) model was developed to express the degree of oxidation of chromite particles as a function of time, temperature and chromite composition. The purpose of this model is therefore to test whether a causal relationship exists rather than for predictive purposes (Allison, 1999). Due to the chemical constraints imposed to maintain charge neutrality in the chromite crystal, the cation concentrations are not fully independent but are correlated, e.g. any fluctuation in $Mg^{2+}$ content results in a fluctuation in $Fe^{2+}$ content in the opposite direction with a similar relationship observed for Cr and Al. Introducing highly correlated explanatory variables in a regression analysis would result in collinearity (Mason and Perreault, 1991), therefore, the Cr and Al contents were considered as a ratio Cr/(Cr + Al), and similarly for Mg and $Fe^{2+}$ the ratio Mg/(Mg + $Fe^{2+}$) was used. The concentrations for $Fe^{3+}$ and Ti were used directly.

As has been done to link spinel composition to reduction behavior (Hunter & Paulson, 1966), a forward selection stepwise regression analysis was performed. This process initiates with no variables in the equation, and variables are then sequentially added with the variable that explains the most variance (while remaining statistically significant) being retained (Judd et al., 2017). This process continues until no more statistically significant ($p < 0.05$) variables can be added. More details regarding the model derivation are provided in the supplementary materials. Fig. 11 shows the results of the stepwise regression, the impact of sequentially increasing the number of independent variables considered on the coefficient of determination ($R^2$) and on the difference in normalized root mean square error (NRMSE) between the experimentally determined oxidation levels and those calculated by the MLR formula.

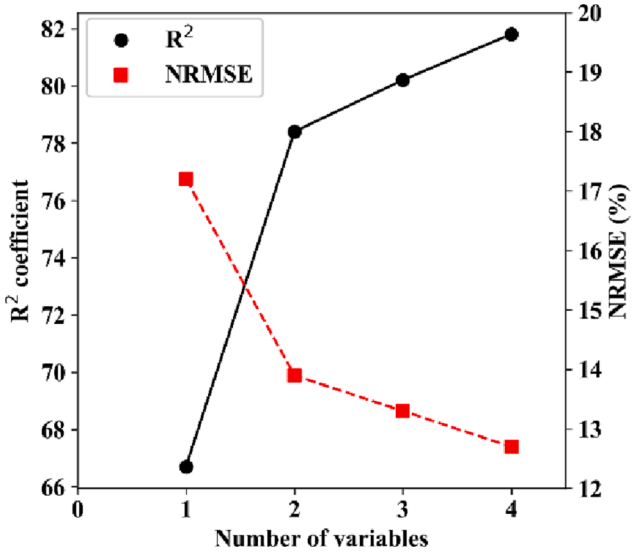


**Fig. 11.** Incremental improvement in coefficient of determination ($R^2$) and the normalized root mean square error (NRMSE) during optimization of the MLR equation as additional variables are considered.

The final model was deemed satisfactory ($R^2 = 0.82$) to explore the relationship between cation composition and the oxidation behavior. The final optimal equation using the aforementioned MLR analyses was determined to be:

$$\alpha = 1.98 + 1.82Ti - 2.06\left(\frac{Cr}{Cr + Al}\right) + 0.23t - 665.80\frac{1}{T} \quad (12)$$

where *Ti*, *Cr*, and *Al* refer to the titanium, chromium and aluminium cation concentrations in the raw spinel as expressed in Table 4, *T* refers to the temperature in Kelvin, and *t* the time in minutes. Regarding the Cr and Al factor, it is known that the Cr content of natural spinels affects the occupancy of Al in the tetrahedral site at high temperatures (Martignago et al., 2003), and has an inhibitive effect. Suzuki et al. (2008) found that the interdiffusion coefficient of Cr-Al in chromite was a function of the Cr/(Cr + Al) ratio, supporting the structure of the equation derived here. Titanium content has a positive coefficient, indicating that it may enhance oxidation rate. The mechanism for this is likely linked to how the tetravalent $Ti^{4+}$ is accommodated in the spinel to maintain charge neutrality. In order to replace a trivalent cation ($Al^{3+}$,$Cr^{3+}$) by a tetravalent cation ($Ti^{4+}$), an additional trivalent cation needs to be replaced by a divalent cation ($Mg^{2+}$) to have an effective charge of $(Mg + Ti)^{3+}$ (De Villiers et al., 2020; Lodha et al., 2011). $Ti^{4+}$ doping of crystals with spinel structure has also been shown to influence structural stability and electrical conductivity of spinels (Deng et al., 2016; Yang et al., 2019), while the strong octahedral preference of $Ti^{4+}$ also favors the transition to an inverse spinel structure during the transformation of chromite to magnetite (Della Giusta et al., 2011). In agreement with work that was performed to study the ultimate extent of sesquioxidation achievable for South African chromites, it was found that the relative concentrations of Cr and Al cations in the spinel were determining factors when oxidation exposure was extended up to four hours (Swanepoel et al., 2022). The $Ti^{4+}$ content was, however, not prominent in estimating the extent of oxidation achievable in the abovementioned work, suggesting that a higher $Ti^{4+}$ content may enhance the kinetics of the oxidation reaction but may not necessarily increase the ultimate extent of oxidation achievable. The $Ti^{4+}$ content of chromites may be beneficial to processes that target short contact times, such as flash roasting or fluidised bed technologies (Yu et al., 2020), while this benefit may be less pronounced in conventional steel belt processes where time at peak reaction temperature is estimated at approximately 10 min (Swanepoel et al., 2022).

### 4.4. Industrial considerations

Although the *iso*-conversional analysis was not able to illuminate which cation(s) dictate(s) the oxidation kinetics of the chromites, it was found that the overriding oxidation kinetics varied across the three ores studied. Contour maps were drawn based on the oxidation fraction data from Fig. 2. Fig. 12 shows how the oxidation varies over time and temperature for the ores, which can assist in selecting an initial operating envelope on an industrial scale from which to start optimizing the oxidation process. For example, the lower temperatures and moderate times needed for UG ore to achieve 90% oxidation may make it suitable for solar pre-oxidation technology routes (Hockaday, 2019; Hockaday et al., 2018). Additionally, in industrial sinter belt operations, there is periodically a need to restrict operating temperatures due to refractory or steel belt integrity requirements. In such instances, depending on the extent of the required temperature reduction, producers may choose to feed a concentrate that can still achieve targeted oxidation rates at the reduced temperatures.

## 5. Conclusions

Three commercial chromite concentrates from South Africa were subjected to isothermal roasting experiments between 873 K and 1473 K (600 °C to 1200 °C), using thermogravimetric analysis to determine the

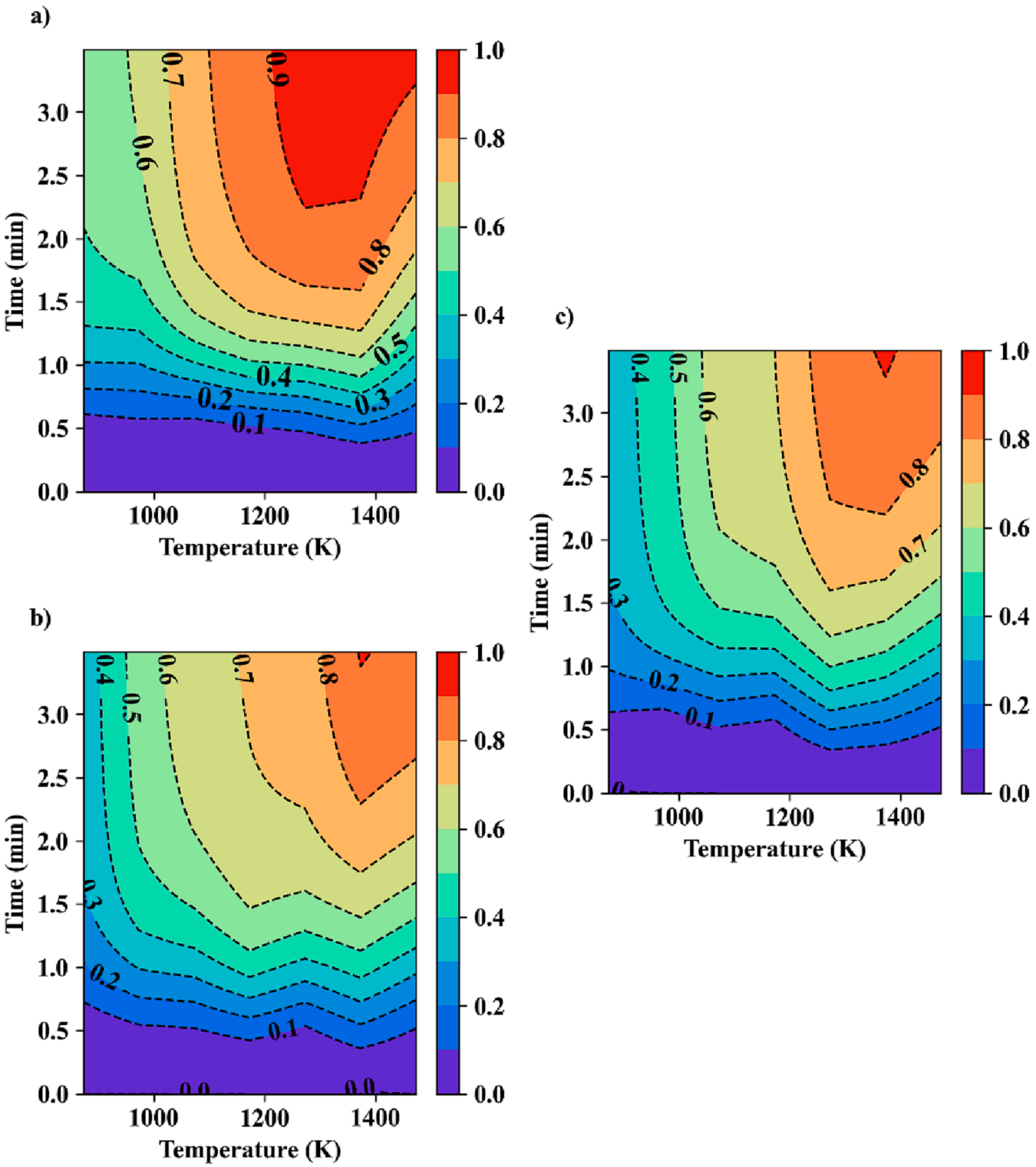


**Fig. 12.** Contour maps of changes in oxidation degree (α) with time and temperature for (a) UG, (b) MG, and (c) LG concentrates.

effect of composition, time and temperature. The following conclusions could be drawn:

Oxidative roasting results in the formation of a sesquioxide phase for all of the ores examined.

This sesquioxide phase crystallizes in a characteristic Widmanstätten pattern; while pores formed in the chromite grains that were not observed prior to roasting.

The Avrami-Erofeev plots revealed that no single mechanism could describe the oxidation process over the entire temperature range; rather a two-stage process was observed. Kinetic exponents of the first stage conform to random nucleation and subsequent growth mechanisms ($n > 1.5$) over the entire explored temperature range. The exponents of the second stage are closest to a three-dimensional diffusion model ($n < 0.6$) between 873 K and 1273 K. In general, the

rate of oxidation was fastest for the UG ore (with the highest Ti content) and slowest for the MG ore (with the highest Cr:Al ratio). Effective $E_\alpha$ was evaluated using the Friedman *iso*-conversional method, confirming that multiple mechanisms are at play in parallel during chromite oxidation. Distinct activation energies being observed between 873 K and 1173 K, as well as in the temperature range of 1173 K and 1473 K. The values obtained for $E_\alpha$ vs α, are in general in agreement with a staged oxidation process as proposed by Da Silva et al. (1976). These stages include the oxidation of $Fe^{2+}$ in a tetrahedral site between 673 K and 973 K (E = 16.7 kJ/mol), the diffusion of $Fe^{3+}$ from octahedral to tetrahedral sites between 973 K and 1173 K (71.1 kJ/mol), and the diffusion of $Fe^{3+}$ from tetrahedral to octahedral sites between 973 K and 1173 K (196.6 kJ/mol).

The activation energies required for $Cr^{3+}$, $Al^{3+}$ and $O^{2-}$ diffusion in a spinel at the examined temperatures are substantially larger than the activation energies calculated for this study, and are therefore estimated to play a limited role in determining the rate limiting steps during oxidation of South African chromites.

A causal regression model was developed to explore the effect of chemical composition on oxidation rate. The results indicate that the ratio of Cr/(Cr + Al) in the chromite spinel has an inhibitory effect on the oxidation rate, while the $Ti^{4+}$ rate has a positive effect and enhances the achieved oxidation rate.

## CRediT authorship contribution statement

**Stefan Swanepoel:** Conceptualization, Funding acquisition, Investigation, Methodology, Analysis, Writing – original draft and editing. **Andrie Garbers-Craig:** Supervision, Validation, Writing – review and editing.

## Declaration of Competing Interest

The authors declare the following financial interests/personal relationships which may be considered as potential competing interests: Stefan Swanepoel reports financial support was provided by Samancor Chrome.

## Data availability

Data will be made available on request.

## Acknowledgments

The authors thank and acknowledge Samancor Chrome for financial assistance toward this research as well as supplying the ore samples. A word of thanks also goes to colleagues and analytical staff in the Department of Materials Science and Metallurgical Engineering at the University of Pretoria.

## Appendix A. Supplementary material

Supplementary data to this article can be found online at https://doi.org/10.1016/j.mineng.2023.108263.

## References

Ajersch, F., 1987. Chemical and physical characteristics affecting the reduction kinetics of iron oxide pellets with solid carbon. Can. Metall. Q. 26 (2), 137–144.
Allison, P.D., 1999. Multiple regression: A primer. Pine Forge Press.
Amores, J.M.G., Escribano, V.S., Busca, G., 1999. Characterisation of Fe–Cr–Al mixed oxides. Mater. Chem. Phys. 60 (2), 168–176.
Atkinson, A., Taylor, R., 1985. Diffusion of 55Fe in Fe2O3 single crystals. J. Phys. Chem. Solid 46 (4), 469–475.
Bachmann, K., Menzel, P., Tolosana-Delgado, R., Schmidt, C., Hill, M., Gutzmer, J., 2019. Multivariate geochemical classification of chromitite layers in the Bushveld Complex, South Africa. Appl. Geochem. 103, 106–117.
Basson, J., Daavittila, J., 2013. Handbook of Ferroalloys: Chapter 9. High Carbon Ferrochrome Technology. Elsevier Inc. Chapters.
Beukes, J., Dawson, N., Van Zyl, P., 2010. Theoretical and practical aspects of Cr (VI) in the South African ferrochrome industry. J. South Afr. Inst. Min. Metall. 110 (12), 743–750.
Biswas, A., Konar, B., Kapure, G.U., Sahu, N., Paliwal, M., 2018. Pre-oxidation treatment of Indian chromite ores: kinetics and phase transformation behavior relevant to ferrochrome manufacturing and pelletization. Miner. Process. Extractive Metall. 1–11 https://doi.org/10.1080/25726641.2018.1515000.
Bonalde, A., Henriquez, A., Manrique, M., 2005. Kinetic analysis of the iron oxide reduction using hydrogen-carbon monoxide mixtures as reducing agent. ISIJ Int. 45 (9), 1255–1260.
Borra, C.R., Kapure, G., Tathavadkar, V., 2010. Investigation of Pre-oxidation of Sukinda Chromite Ore Tata Search. J. Technol. Adv. Tata Steel 1, 145–148.
Brown, M.E., 2001. Introduction to thermal analysis: techniques and applications. Springer.
Brown, M.E., Dollimore, D., Galwey, A.K., 1980. Reactions in the solid state, Vol. 22. Elsevier.
Cho, H.J., Pistorius, P.C., 2011. The Effects of Concentrate Source and Particle Size on Oxidation Behavior of Magnetite AISTech 2011 Proceedings, Warrendale, PA.
Christian, J.W., 2002. The theory of transformations in metals and alloys (3 ed.). Pergamon.
Colombo, U., Fagherazzi, G., Gazzarrini, F., Lanzavecchia, G., Sironi, G., 1964. Mechanisms in the first stage of oxidation of magnetites. Nature 202 (4928), 175–176.
Cramer, L.A., Basson, J., Nelson, L.R., 2004. The impact of platinum production from UG2 ore on ferrochrome production in South Africa. J. S. Afr. Inst. Min. Metall. 104 (9), 517–527.
Da Silva, E.G., Abras, A., Camara, A.S., 1976. Mössbauer effect study of cation distribution in natural chromites. Le Journal de Physique Colloques 37 (C6), 783–785.
De Villiers, J.P., Mulange, D., Garbers-Craig, A.M., 2020. The Effect of Titanium Oxide Additions on the Phase Chemistry and Properties of Chromite-Magnesia Refractories. Ceramics 3 (1), 127–143.
Della Giusta, A., Carbonin, S., Russo, U., 2011. Chromite to magnetite transformation: compositional variations and cation distributions (southern Aosta Valley, Western Alps, Italy). Periodico di Mineralogia 80 (1), 1–17.
Deng, J., Xu, Y., Xiong, L., Li, L., Sun, X., Zhang, Y., 2016. Improving the fast discharge performance of high-voltage LiNi0. 5Mn1. 5O4 spinel by Cu2+, Al3+, Ti4+ tri-doping. J. Alloy. Compd. 677, 18–26.
Dimitra, K., Konstantinos, C., 2021. Nonisothermal crystallization kinetics: studying the validity of different Johnson–Mehl–Avrami–Erofeev–Kolmogorov (JMAEK) based equations. Thermochim. Acta 704.
Dishwar, R.K., Agrawal, S., Mandal, A.K., Sinha, O., 2020. Smelting process of chromite ore fines to produce crude Fe–Cr–Ni–N Alloy. Trans. Indian Inst. Met. 73 (3), 537–542.
Doebelin, N., Kleeberg, R., 2015. Profex: a graphical user interface for the Rietveld refinement program BGMN. J. Appl. Cryst. 48 (5), 1573–1580.
Dowdy, D., 1987. Meaningful activation energies for complex systems. J. Therm. Anal. 32 (1), 137–147.
Dowdy, D., 1987. Meaningful activation energies for complex systems II: Evaluation of the Friedman method when applied to multiple reactions, and comparison with the Ozawa-Flynn-Wall method. J. Therm. Anal. Calorim. 32 (4), 1177–1187.
Droop, G., 1987. A general equation for estimating Fe3+ concentrations in ferromagnesian silicates and oxides from microprobe analyses, using stoichiometric criteria. Mineral. Mag. 51 (361), 431–435.
Du Preez, S., Beukes, J., Paktunc, D., Van Zyl, P., Jordaan, A., 2019. Recycling pre-oxidized chromite fines in the oxidative sintered pellet production process. J. South Afr. Inst. Min. Metall. 119 (2), 207–215.
Elder, J., 1984. Multiple reaction scheme modelling. I: Independent and competitive first order reactions. J. Therm. Anal. 29 (6), 1327–1342.
Elder, J., 1990. A comment on mathematical expressions used in solid state reaction kinetics studies by thermal analysis. Thermochim Acta 171, 77–85.
Erasmus, L.J., 1995. Induration of Chromite Infacon 7. Trondheim, Norway.
Fanfoni, M., Tomellini, M., 1998. The Johnson-Mehl-Avrami-Kohnogorov model: a brief review. Il. Nuovo Cimento D 20 (7), 1171–1182.
Ferracutti, G.R., Gargiulo, M.F., Ganuza, M.L., Bjerg, E.A., Castro, S.M., 2015. Determination of the spinel group end-members based on electron microprobe analyses. Mineral. Petrol. 109 (2), 153–160.
Flynn, J.H., Wall, L.A., 1966. General treatment of the thermogravimetry of polymers. J. Res. Natl. Bureau Standards Section A, Phys. Chem. 70 (6), 487.
Friedman, H.L., 1964. Kinetics of thermal degradation of char-forming plastics from thermogravimetry. Application to a phenolic plastic. J. Polym. Sci., Part C: Polym. Symp. 6 (1), 183–195.
Gall, M.L., Lesage, B., Bernardini, J., 1994. Self-diffusion in α-Al2O3 I. Aluminium diffusion in single crystals. Philos. Mag. A 70 (5), 761–773.
Galwey, A.K., 2003. What is meant by the term 'variable activation energy'when applied in the kinetic analyses of solid state decompositions (crystolysis reactions)? Thermochim Acta 397 (1–2), 249–268.
Galwey, A.K., Brown, M.E., 2002. Application of the Arrhenius equation to solid state kinetics: can this be justified? Thermochim Acta 386 (1), 91–98.
Garn, P., 1988. Kinetics of decomposition of the solid state: is there really a dichotomy? Thermochim Acta 135, 71–77.
Ghafarinazari, A., Zera, E., Lion, A., Scarpa, M., Sorarù, G.D., Mariotto, G., Daldosso, N., 2016. Isoconversional kinetics of thermal oxidation of mesoporous silicon. Thermochim Acta 623, 65–71.

Gilewicz-Wolter, J., Żurek, Z., Dudala, J., Lis, J., Homa, M., Wolter, M., 2006. Diffusion Rates of 51Cr, 54Mn and 59Fe in MnCr2O4 and FeCr2O4 Spinels. Adv. Sci. Technol. 46, 27–31.
Gillot, B., Ferriot, J.-F., Dupré, G., Rousset, A., 1976. Study of the oxidation kinetics of finely-divided magnetites. II-Influence of chromium substitution. Mater. Res. Bull. 11 (7), 843–849.
Gillot, B., Bouton, F., Chassagneux, F., Rousset, A., 1980. Study of the oxidation kinetics of finely-divided magnetites III—Influence of chromium and aluminum substitution. Mater. Res. Bull. 15 (1), 1–7.
Gillot, B., Jemmali, F., Rousset, A., 1986. Kinetics and mechanism of ferrous spinel oxidation studied by electrical conductivity and thermogravimetry. J. Mater. Sci. 21 (12), 4436–4442.
Gillot, B., El Guendouzi, M., Kharroubi, M., Tailhades, P., Metz, R., Rousset, A., 1989. Phase transformation-related kinetic in the oxidation of a manganese mixed oxide with a spinel structure. Mater. Chem. Phys. 24 (1–2), 199–208.
Gorbachev, V., 1981. To the problem of applying the equation of Kolmogorov, Erofeev, Kazeev, Avrami and Mampel to the kinetics of non-isothermal transformations. J. Therm. Anal. 20 (2), 483–485.
Gotor, F.J., Criado, J.M., Malek, J., Koga, N., 2000. Kinetic analysis of solid-state reactions: the universality of master plots for analyzing isothermal and nonisothermal experiments. Chem. A Eur. J. 104 (46), 10777–10782.
Haas, L.A., Nigro, J.C., Moe, R.C., 1993). Use of oxygen-enriched gas for the oxidation of acid and fluxed taconite pellets, Vol. 9473. US Department of Interior, Bureau of Mines.
Hancock, J., Sharp, J., 1972. Method of comparing solid-state kinetic data and its application to the decomposition of kaolinite, brucite, and BaCO3. J. Am. Ceram. Soc. 55 (2), 74–77.
Hockaday, L., 2019. Solar thermal applications in minerals processing in South Africa. In: 6th South African solar energy conference. East London, South Africa.
Hockaday, S., Dinter, F., Harms, T., 2018. Introducing solar thermal heat into minerals processing: A case study on replacing a diesel burner at a sinter plant. SASEC2018 (submitted), 74-78.
Hunter, W.L., Paulson, D.L., 1966. Carbon reduction of chromite. US Department of the Interior, Bureau of Mines.
Jiang, T., Zhang, Y., Huang, Z., Li, G., Fan, X., 2008. Preheating and roasting characteristics of hematite–magnetite (H–M) concentrate pellets. Ironmak. Steelmak. 35 (1), 21–26.
Judd, C.M., McClelland, G.H., Ryan, C.S., 2017. Data analysis: A model comparison approach to regression, ANOVA, and beyond. Routledge.
Kapure, G., Tathavadkar, V., Rao, C. B., Rao, S. M., & Raju, K. S. (2010). Coal based direct reduction of preoxidized chromite ore at high temperature. The Twelfth International Ferroalloys Congress: Sustainable Future, Helsinki, Finland.
Kharbish, S., 2018. Raman spectroscopic features of Al-Fe3+-poor magnesiochromite and Fe2+-Fe3+-rich ferrian chromite solid solutions. Mineral. Petrol. 112 (2), 245–256.
Khawam, A., Flanagan, D.R., 2005. Role of isoconversional methods in varying activation energies of solid-state kinetics: I. Isothermal kinetic studies. Thermochim. Acta 429 (1), 93–102.
Khawam, A., Flanagan, D.R., 2006. Basics and applications of solid-state kinetics: a pharmaceutical perspective. J. Pharm. Sci. 95 (3), 472–498.
Khawam, A., Flanagan, D.R., 2006. Solid-state kinetic models: basics and mathematical fundamentals. J. Phys. Chem. B 110 (35), 17315–17328.
Kleynhans, E., Beukes, J., Van Zyl, P., Fick, J., 2017. Techno-economic feasibility of a pre-oxidation process to enhance prereduction of chromite. J. South Afr. Inst. Min. Metall. 117 (5), 457–468.
Kleynhans, E.L.J., Neizel, B.W., Beukes, J.P., van Zyl, P.G., 2016. Utilisation of pre-oxidised ore in the pelletised chromite pre-reduction process. Miner. Eng. 92, 114–124. https://doi.org/10.1016/j.mineng.2016.03.005.
Koleli, N., Demir, A., 2016. Chromite. In: Prasad, M.N.V. (Ed.), Environmental Materials and Waste. Academic Press, pp. 245–263.
Krüger, P., 1993. On the relation between non-isothermal and isothermal Kolmogorov-Johnson-Mehl-Avrami crystallization kinetics. J. Phys. Chem. Solid 54 (11), 1549–1555.
Lesage, B., Huntz, A., Petot-Ervas, G., 1983. Transport phenomena in undoped and chromium or yttrium doped-alumina. Radiat. Eff. 75 (1–4), 283–299.
Lodha, R., Oprea, G., Troczynski, T., 2011. Role of Ti4+ and Sn4+ ions in spinel formation and reactive sintering of magnesia-rich ceramics. Ceram. Int. 37 (2), 465–470.
Logan, S., 1982. The origin and status of the Arrhenius equation. J. Chem. Educ. 59 (4), 279.
Lughi, V., Lenaz, D., Bonifacio, A., Princivalle, F., Sergo, V., Parisi, F., 2020. A Raman spectroscopy study of the oxidation processes in synthetic chromite FeCr2O4. Ceram. Int. 46 (18), 29382–29387.
Lv, W., Lv, X., Zhang, Y., Li, S., Tang, K., Song, B., 2017. Isothermal oxidation kinetics of ilmenite concentrate powder from Panzhihua in air. Powder Technol. 320, 239–248. https://doi.org/10.1016/j.powtec.2017.07.058.
Martignago, F., Negro, A.D., Carbonin, S., 2003. How Cr3+ and Fe3+ affect Mg–Al order–disorder transformation at high temperature in natural spinels. Phys. Chem. Miner. 30 (7), 401–408.
Mason, C.H., Perreault Jr, W.D., 1991. Collinearity, power, and interpretation of multiple regression analysis. J. Mark. Res. 28 (3), 268–280.
Monazam, E.R., Breault, R.W., Siriwardane, R., 2014. Kinetics of magnetite (Fe3O4) oxidation to hematite (Fe2O3) in air for chemical looping combustion. Ind. Eng. Chem. Res. 53 (34), 13320–13328.
Moya, E., Moya, F., Sami, A., Juve, D., Treheux, D., Grattepain, C., 1995. Diffusion of chromium in alumina single crystals. Philos. Mag. A 72 (4), 861–870.
Muraleedharan Nair, M., Abanades, S., 2021. Solid-State Reoxidation Kinetics of A/B-Site Substituted LaMnO3 During Solar Thermochemical CO2 Conversion. Energ. Technol. 9 (2), 2000885.
Paladino, A.E., Kingery, W., 1962. Aluminum ion diffusion in aluminum oxide. J. Chem. Phys. 37 (5), 957–962.
Patnaik, A.S., Goldfarb, J.L., 2016. Continuous activation energy representation of the Arrhenius equation for the pyrolysis of cellulosic materials: feed corn stover and cocoa shell biomass. Cellulose Chem. Technol. 50 (2), 311–320.
Peleg, M., Normand, M.D., Corradini, M.G., 2012. The Arrhenius equation revisited. Crit. Rev. Food Sci. Nutr. 52 (9), 830–851.
Posner, E.S., Ganguly, J., Hervig, R., 2016. Diffusion kinetics of Cr in spinel: Experimental studies and implications for 53Mn–53Cr cosmochronology. Geochim. Cosmochim. Acta 175, 20–35.
Prot, D., Monty, C., 1996. Self-diffusion in α-Al2O3. II. Oxygen diffusion in 'undoped'single crystals. Philos. Mag. A 73 (4), 899–917.
Qu, Y., Yang, Y., Zou, Z., Zeilstra, C., Meijer, K., Boom, R., 2014. Thermal decomposition behaviour of fine iron ore particles. ISIJ Int. 54 (10), 2196–2205.
Reddy, K., Cooper, A.R., 1983. Oxygen Diffusion in MgO and α-Fe2O3. J. Am. Ceram. Soc. 66 (9), 664–666.
Rothhaar, U., Oechsner, H., 1998. Interdiffusion studies of Cr2O3 layers on ceramic Al2O3 substrates. Thin Solid Films 324 (1–2), 165–169.
Sabioni, A., Huntz, A., Millot, F., Monty, C., 1992. Self-diffusion in Cr2O3 II. Oxygen diffusion in single crystals. Philos. Mag. A 66 (3), 351–360.
Sabioni, A., Lesage, B., Huntz, A., Pivin, J., Monty, C., 1992. Self-diffusion in Cr2O3 I. Chromium diffusion in single crystals. Philos. Mag. A 66 (3), 333–350.
Salmani, M., Alamdari, E.K., Firoozi, S., 2017. Isoconversional analysis of thermal dissociation kinetics of hematite in air and inert atmospheres. J. Therm. Anal. Calorim. 128 (3), 1385–1390.
Sandeep Kumar, T., Viswanathan, N., Ahmed, H., Dahlin, A., Andersson, C., Bjorkman, B., 2019. Investigation of magnetite oxidation kinetics at the particle scale. Metall. Mater. Trans. B 50 (1), 150–161. https://doi.org/10.1007/s11663-018-1459-5.
Sardari, A., Alamdari, E.K., Noaparast, M., Shafaei, S.Z., 2017. Kinetics of magnetite oxidation under non-isothermal conditions. Int. J. Miner. Metall. Mater. 24 (5), 486–492. https://doi.org/10.1007/s12613-017-1429-y.
Šesták, J., Berggren, G., 1971. Study of the kinetics of the mechanism of solid-state reactions at increasing temperatures. Thermochim Acta 3 (1), 1–12.
Sheu, H.-H., Hsiung, L.-C., Sheu, J.-R., 2009. Synthesis of multiphase intermetallic compounds by mechanical alloying in Ni–Al–Ti system. J. Alloy. Compd. 469 (1–2), 483–487.
Stubican, V., Osenbach, J., 1984. Influence of anisotropy and doping on grain boundary diffusion in oxide systems. Solid State Ion. 12, 375–381.
Sun, R., 1958. Diffusion of cobalt and chromium in chromite spinel. J. Chem. Phys. 28 (2), 290–293.
Suzuki, A., Yasuda, A., Ozawa, K., 2008. Cr and Al diffusion in chromite spinel: experimental determination and its implication for diffusion creep. Phys. Chem. Miner. 35 (8), 433–445.
Swanepoel, S., Garbers-Craig, A.M., De Villiers, J.P.R., 2022. The oxidation behavior of a selection of South African chromites. Mater. Metall. Trans. B 53, 3805–3824. https://doi.org/10.1007/s11663-022-02643-x.
Tang, M., Cho, H.J., Pistorius, P.C., 2014. Early gaseous oxygen enrichment to enhance magnetite pellet oxidation. Metall. Mater. Trans. B 45, 1304–1314.
Tathavakar, V.D., Antony, M., Jha, A., 2005. The physical chemistry of thermal decomposition of South African chromite minerals. Metall. Mater. Trans. B 36 (1), 75–84.
Thackeray, M., Mansuetto, M., Dees, D., Vissers, D., 1996. The thermal stability of lithium-manganese-oxide spinel phases. Mater. Res. Bull. 31 (2), 133–140.
Treffner, W.S., 1961. Behavior of chromite spinel as related to microstructure. J. Am. Ceram. Soc. 44 (12), 583–591.
Vyazovkin, S., 2016. A time to search: finding the meaning of variable activation energy. Phys. Chem. Chem. Phys. 18 (28), 18643–18656.
Vyazovkin, S., Lesnikovich, A., 1990. An approach to the solution of the inverse kinetic problem in the case of complex processes: Part 1. Methods employing a series of thermoanalytical curves. Thermochim Acta 165 (2), 273–280.
Vyazovkin, S., Burnham, A.K., Criado, J.M., Pérez-Maqueda, L.A., Popescu, C., Sbirrazzuoli, N., 2011. ICTAC Kinetics Committee recommendations for performing kinetic computations on thermal analysis data. Thermochim Acta 520 (1–2), 1–19.
Vyazovkin, S., Wight, C., 1997. Kinetics in solids. Annu. Rev. Phys. Chem. 48 (1), 125–149.
Vyazovkin, S., Wight, C.A., 1999. Model-free and model-fitting approaches to kinetic analysis of isothermal and nonisothermal data. Thermochim Acta 340, 53–68.
Vyazovkin, S., Bogdanova, V., Klimovtsova, I., Lesnikovich, A., 1991. Invariant kinetic parameters of polymer thermolysis. III. The influence of a fire-retardant additive on polypropylene thermolysis. J. Appl. Polym. Sci. 42 (7), 2095–2098.
Wolfinger, T., Spreitzer, D., Zheng, H., Schenk, J., 2022. Influence of a Prior Oxidation on the Reduction Behavior of Magnetite Iron Ore Ultra-Fines Using Hydrogen. Metall. Mater. Trans. B 53 (1), 14–28. https://doi.org/10.1007/s11663-021-02378-1.
Xing, L., Qu, Y., Wang, C., Shao, L., Zou, Z., Song, W., 2020. Kinetic study on thermal decomposition behavior of hematite ore fines at high temperature. Metall. Mater. Trans. B 51 (1), 395–406.
Yang, Z., Wang, Y., Chen, X., Wu, H., Zhang, Y., 2019. Mg2+ and Ti4+ co–doped spinel LiMn2O4 as lithium-ion battery cathode. ChemistrySelect 4 (33), 9583–9589.
Ye, M.-f., & Wu, G.-l. (2018). Preparation of Oxidized Pellets with Chrome Ore 9th International Symposium on High-Temperature Metallurgical processing, 775-784. Doi:10.1007/978-3-319-72138-5_74.

Yu, J., Han, Y., Li, Y., Gao, P., 2020. Recent advances in magnetization roasting of refractory iron ores: A technological review in the past decade. Miner. Process. Extr. Metall. Rev. 41 (5), 349–359.
Yu, D., Paktunc, D., 2018. Direct production of ferrochrome by segregation reduction of chromite in the presence of calcium chloride. Metals 8 (1), 69.
Zhao, B., & Hayes, P. C. (2010). Effects of oxidation on the microstructure and reduction of chromite pellets. Proceedings of the 12th International Ferroalloys Congress: Sustainable Future, Helsinki, Finland.
Zhou, Y., Jin, X., Mukovskii, Y., Shvets, I., 2003. Kinetics of oxidation of low-index surfaces of magnetite. J. Phys. Condens. Matter 16 (1), 1.
Zhu, D., Yang, C., Pan, J., Li, X., 2016. Comparison of the Oxidation Behaviors of High FeO Chromite and Magnetite Concentrates Relevant to the Induration of Ferrous Pellets. Metall. Mater. Trans. B 47 (5), 2919–2930. https://doi.org/10.1007/s11663-016-0770-2.
Zhu, D., Yang, C., Pan, J., Zhang, Q., Shi, B., Zhang, F., 2016. Insight into the Consolidation Mechanism of Oxidized Pellets Made from the Mixture of Magnetite and Chromite Concentrates. Metall. Mater. Trans. B 47 (2), 1010–1023. https://doi.org/10.1007/s11663-015-0553-1.